NASA
Technical
Paper
3442

December 1993

Analysis and Test of Low Profile Aluminum Aerospace Tank Dome

R. Ahmed
and J.M. Wilhelm

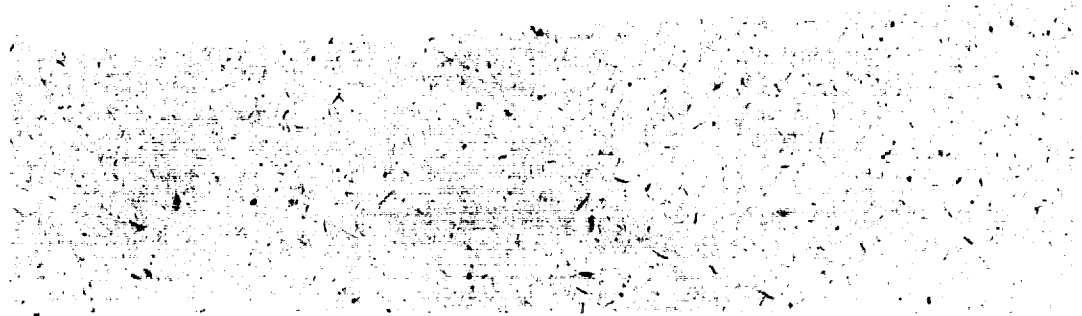

TABLE OF CONTENTS

LIST OF ILLUSTRATIONS

LIST OF ILLUSTRATIONS (Continued)

LIST OF TABLES

TECHNICAL PAPER

ANALYSIS AND TEST OF LOW-PROFILE ALUMINUM AEROSPACE TANK DOME

I. INTRODUCTION

In order to increase the structural performance of cryogenic tanks, the aerospace industry is beginning to employ low-profile bulkheads in new-generation launch vehicle designs. A low-profile dome has a major-to-minor radius ratio greater than $\sqrt{2}$ and offers possibilities for increased performance over existing designs by maximizing the volume of a tank for a given length. That is, the shortened adapter structure allows for either a greater usable propellant volume with an unchanged vehicle length or for a shorter overall vehicle length with an unchanged propellant volume. Low-profile designs have been avoided in traditional aerospace designs because the domes experience hoop compression at locations near the interface with the tank cylindrical portion when loaded under internal pressure. Since circumferential buckling can then occur, low-profile designs require stiffening of the hoop compression region either by adding circumferential ribs or by increasing local thicknesses. In the past, closed-form solutions were used to analyze the domes, and uncertainty factors were imposed because of the inability to accurately predict the onset of buckling. Consequently, the low-profile domes were much heavier than the $\sqrt{2}$ domes. Today, better analytical tools are available. The low-profile contours can be defined by a design optimizer which is no longer limited to closed-form solutions. State-of-the-art finite difference and finite element analysis codes can also be used to more accurately predict the onset of buckling, eliminating the need for uncertainty factors and resulting in a lower weight design. The resulting system performance impact is that heavy adapter structure is displaced with only a slight increase in bulkhead weight.

Since limited data are available on buckling of stiffened, variable thickness domes, a joint test program was conducted by Marshall Space Flight Center (MSFC) and General Dynamics Space Systems Division (GDSSD) using a subscale low-profile 2219 aluminum dome. The 2219 subscale dome program was part of the joint NASA/MSFC and GDSSD Cryogenic Tank Technology Program (CTTP) for the development of advanced cryogenic tank manufacturing processes incorporating aluminum lithium. The 2219 dome served as a pathfinder for development and test of future low-profile aluminum lithium dome designs. This report describes the analysis, test, and results of the 2219 dome project.

A. Purpose

The objectives of the subscale dome test were as follows:

1. Demonstrate the feasibility of the low profile spin formed design

2. Verify advanced analysis tools (finite element models and hand analysis) by comparing analytical predictions with test data. The validated analytical tools will then be available for structural design and analysis of future low-profile domes (especially those of aluminum-lithium construction)

3. Investigate capabilities of advanced nondestructive evaluation (NDE) methods such as laser shearography, digital image correlation, and acoustic emission.

B. Summary

This report presents analysis and test data from the subscale dome tests. Strain gauge and displacement readings are compared with analytical predictions. Assessments of the article's strength and resistance to buckling are given.

II. LOW-PROFILE 2219 DOME TEST

The low-profile aluminum dome tests were conducted from February 17, 1993, to February 19, 1993, under the supervision of ED71 (MSFC Structural Test Division).

A. Test Article Description

Manufactured by Spin Craft Corporation, the 2219-T6 test article was a low-profile 1.976 to 1 elliptical subscale dome of 51.55-inch nominal inside (major) diameter and a height of 16.07 inches (fig. 1). The various shell parts were first welded together to form a blank, thick spin formed to the desired elliptical shape, solution heat treated and quenched, aged, final machined, and finally chemically milled to within the required dimensional tolerances. Three stiffening rings were machined into the final configuration (near the dome equator) to resist hoop buckling. Stepped regions were added near the welds to distribute loads and minimize weld stress concentrations. During the manufacturing process, a deep circumferential groove was accidentally cut into the dome skin near the cover plate interface. The dome was repaired with an adhesively bonded doubler plate of 0.063-inch thickness.

Using reduced skin gauge thicknesses, the dome was biased to fail in the 90° section instrumented for the test. The test quadrant had thick weld lands around the 0° and 90° meridional welds and around the dome to adapter ring weld, transitioning to thinner nominal thicknesses in the middle. Typical skin gauge thicknesses in the dome ranged from 0.022 to 0.037 inch and the stiffeners had a nominal thickness of 0.020 inch. The dome design pressures were 30 psig (limit), 37.5 psig (proof), and 45 psig (ultimate).

B. Test Fixture Description

The test fixture consisted of three basic components: a cover plate, a dome base plate, and a circumferential clamp to secure the test article to the base plate. The cover plate was attached by 16 bolts to the top of the dome and contained the water connections and pressure fittings for both nominal pressure and pressure relief, as well as an instrumentation feed-through for wires from the inside strain gauges. The clamp secured the dome adapter ring to the base plate and was sealed with a Gore Tex™ strip to prevent water leakage under the maximum expected pressure.

C. Pressure Loading Description

The Structural Test Division's facilities water supply was the hydrostatic pressure source. The pressure was controlled manually from a control panel that had over-pressure and vacuum pressure relief valves to preclude inadvertent damage to the test article before the test objectives were accomplished.

In the first attempt to fail the dome, the water supply pressure of 62 psi was insufficient to buckle or rupture the article. Testing resumed the following day using a supplemental pump to create sufficient hydrostatic pressure to buckle and rupture the dome.

D. Instrumentation and Equipment

The dome was instrumented by the MSFC Structural Test Division with pressure transducers, strain gauges, displacement gauges, and acoustic emission transducers. Additionally, laser shearography and digital image correlation techniques were used to detect buckling, complementing the conventional strain gauge and displacement readings.

The pressure transducers were mounted on the dome near the connection fittings and consisted of analog dials at the test control station and digital readings for the data acquisition system (DAS).

Four groups of biaxial strain gauges were arranged with gauges mounted on the inside and outside of the shell (back-to-back) at each location. Gauges were placed along three meridians which were spaced at 10° meridional intervals to verify axisymmetry and to detect the onset of buckling. Another group of gauges was placed on a weld land to monitor the stress distribution there.

Sixteen displacement gauges were mounted (roughly) normal to the surface of the dome along a meridian.

Laser shearography was used on this dome as an optical inspection method that can detect buckling in a structure by displaying the load-induced out-of-plane displacements on a video monitor. The technique was used to monitor displacements in the strain-gauged quadrant. At the time of the test, the laser shearography equipment was not calibrated to give actual numerical results for deflections. Its primary use was to visually detect the onset and development of buckling from the shearographic images.

Another technique used to detect displacements and strains was digital image correlation. Digital image correlation mathematically compares two digitized images of an area in the test quadrant of the dome. One image is of the object before deformation, the second was created after the dome was pressurized. The deformed image was updated at every pressure increment of interest. In-plane deformations and deformation gradients (from which strains were calculated) were then calculated using a personal computer, and the results were displayed on a color monitor. Color plots of displacements and strains as well as precise numerical values at a given point on the surface were available.

Of the three NDE methods investigated, acoustic emissions provided the most accurate indications of the dome response, especially the onset of buckling. Acoustic emission is used to detect acoustic waves generated by microcracks propagating in the dome material as the article is pressurized. Five piezoelectric sensors were placed at various locations around the structure to detect the acoustic events, isolating the crack propagation locations. The amplitude, frequency, and duration of each event was

captured and stored in a computer for subsequent analysis. These three characteristics were used to ascertain the cause of each event (e.g., strain gauge debond, crack propagation, buckling).

E. Test Procedure

The test procedure originally consisted of two load sequences, but was amended to three as a result of contingencies during test operations. The first load sequence was a 0- to 30-psig pressurization to verify strain gauge, extensometer, and other instrumentation readings as well as to check out the entire system. The second part was to be a pressurization from 0 psi to buckling and then to ultimate capability of the dome, but actually went to only 62 psig because of the limitations of the water supply pressure.

The first loading sequence was performed as follows:

1. The system was verified (pressurization configuration, data acquisition system, instrumentation zeros, etc.)

2. The dome was filled with water and pressurized from 0 to 15 psig and vented to 0 psig. Scans were taken at 0, 5, 10, 12, 14, 14.25, 14.5, 14.75, and 15 psig while increasing pressure and decreasing pressure

3. The dome was then pressurized from 0 to 30 psig and back to 0 psig while recording scans at 0, 5, 10, 15, 20, 25, and 30 (again both while increasing and decreasing pressure)

4. The water was drained from the dome.

The second loading sequence was performed as follows:

1. Steps 1 and 2 from the first run were repeated

2. The dome was pressurized from 0 to 30 psig, recording at 0, 5, 10, 15, 20, 25, and 30 psig. After reaching 30 psig, the pressure was increased in 2.5 psig increments to 37.5 psig. The pressure was held at 37.5 psig for 5 min and then vented to 0 psig. All gauges were re-zeroed. Once again the structure was pressurized to 37.5 psig and higher with scans taken at 38, 39, 40, 41, 42, 43, and 44 psig. Pressurization continued until reaching the maximum water supply pressure of 62 psi. Since no buckling or tensile failure had occurred, the system was vented to 0 psig and shut down in order to splice in an auxiliary pump for additional pressure.

The third and final loading sequence was as follows:

The gauges were not re-zeroed in order to keep the readings as consistent as possible with those of the second run. The dome was pressurized from ~0 psig to rupture (72.6 psig) in the following increments: 0, 5, 10, 15, 20, 25, 30, 35, 37.5, 38, 39, 40, 41, and so on up to 62 psig. After 62 psig, the dome was pressurized in 0.25 psig increments to the failure load of 72.6 psig.

F. Results

Figures 2 and 3 show the locations and nomenclature of the deflection and strain gauges, respectively. The deflections as a function of pressure are listed in tables 1 and 2, whereas the strains as a function of pressure are listed in tables 3 and 4. Displacement versus pressure plots are shown in figures 4 through 19 and compare both analysis and test. Figures 20 through 27 show analysis and test strain versus pressure for selected strain gauges. These strains were chosen so that the most critical dome sections could be examined and that both buckling and tensile failure modes would be covered.

III. ANALYSIS MODELS OF TEST SPECIMEN

A. General Dynamics Models

The General Dynamics stress analyst constructed a model of the dome using the industry-accepted BOSOR5 analysis code to predict the onset of buckling and to account for material and geometric nonlinearity. A 10-segment BOSOR5 model of the bulkhead and access door was constructed. The shell wall for the entire 2:1 ellipse was input using the elliptical shell input method. This model was used to verify both the material strength of the hardware and its buckling strength. Several runs were made to search for different ranges of circumferential waves. Figure 28 shows the model configuration.

The bonded doubler plate, the as-built configuration and thicknesses, and MIL-HDBK-5E material allowables were incorporated in the model.

In addition to the BOSOR model, a 45° model of the dome was constructed in NASTRAN to investigate the stresses and deflections in the weld lands. The NASTRAN model was run with a linear analysis (QUAD4 elements) using a weld land of 0.051 inch stepping down to 0.038 inch before reducing to typical thickness.

B. NASA In-House Finite Element Models

Using actual dome gauge thicknesses determined by ultrasonic measurement in the instrumented quadrant of the dome, NASA/MSFC's finite element modeling effort began with construction of a two-dimensional (2–D) axisymmetric ANSYS model (using STIF42 2–D isoparametric elements with 2 degrees of freedom at each node). The model extended meridionally from the outboard edge of the dome cover plate to the tangency point of the adapter ring and was constrained from radial displacement at the dome cap interface and from longitudinal displacement at the bottom of the adapter ring section. The 2–D ANSYS model also incorporated MIL-HDBK-5E 2219-T6 material allowables data. Small displacements were assumed in order to expedite convergence of results. The 2–D model was used to predict biaxial tension failure.

The midplane contour and local thicknesses along one meridian in the instrumented quadrant were used to sweep a 20° section of the dome. These data were translated to an ANSYS three-dimensional (3–D) model, using STIF63 quadrilateral shell elements to predict linear eigenvalue buckling. At the dome cover plate interface and at the bottom of the adapter ring section, the model was constrained from radial and axial rotations and tangential displacements. The cover plate interface was also

constrained from tangential rotations. Symmetry boundary conditions were applied at the 0° and 20° meridional edges. Thirty elements were meshed across the 20° section during the initial analyses.

Analysis attempts with a refined mesh did not converge in ANSYS, so the model was ported to CSA NASTRAN. Applied boundary conditions were the same as for the ANSYS 3–D model. The nodal spacing used was based on results from previous MSFC NASTRAN buckling error studies and effectively doubled the number of nodes in the hoop direction of the ANSYS model. A convergent linear eigenvalue buckling solution resulted. The 3–D ANSYS model was subsequently used for a 3–D nonlinear plasticity solution to successfully verify the 2–D model results.

Figure 29 shows the 3–D NASTRAN buckling model, while figures 30 and 31 show the 3–D and 2–D ANSYS models, respectively.

IV. DISCUSSION

Two primary failure modes exist in a combined tension-compression structure such as this internally pressurized low-profile dome: compressive instability (buckling) and biaxial tensile failure. Both failure modes occurred in this test. When loaded under internal pressure, ellipsoidal shells are insensitive to geometric defects and load eccentricities, eliminating a requirement for a buckling knockdown factor based on a nonlinear buckling solution. Unlike the response when loaded under external pressure, the shells exhibit postbuckling stability.[1] Consequently, the dome ruptured in the biaxial tension area and did not catastrophically fail in the buckled region.

A. Buckling Loads

The 3–D NASTRAN analysis results indicated first mode eigenvalue buckling at 69.5 psig pressure with no knockdown factor. At 69.5 psig, the 20° NASTRAN model exhibited 81 circumferential waves, each with a meridional half-wave, located at and just below the first rib stiffener. The meridional half-wave passed through the stiffener, rolling the stiffener about the tangential axis.

Unlike the NASTRAN analysis, the 2–D BOSOR analysis evaluated the first buckling mode using a nonlinear solution. The lowest eigenvalue was predicted to be in the 62.5 to 65 psig range with 62 circumferential waves (each having a single meridional half-wave). Again, no knockdown factor was applied.

B. Ultimate Tensile Failure Load

Ultimate tensile failure was predicted by both the 2–D axisymmetric nonlinear and the 3–D nonlinear ANSYS analyses to occur between 72 and 74 psig. The failure region was isolated by both models to be in the region between the third stiffener from the equator and the doubler plate (fig. 1). The analysis assumed MIL-HDBK-5E properties of 36-ksi yield strength and 54-ksi ultimate strength for 2219-T6 aluminum. The actual failure occurred at 72.6 psig, correlating well with the prediction. The specimen after failure is shown in figure 32. A closeup view of the failed area is shown in figure 33.

C. Comparison of Test and Analysis

The discussion of nonbuckling test results versus analysis is valid only at pressures below the level of incipient buckling, in the linear region up to 55 to 60 psi, since the 2–D and 3–D stress analyses did not account for strains in the (nonlinear) buckling regime.

As mentioned previously, figures 4 through 19 show analysis and test deflections versus pressure, while analysis and test strains are shown in figures 20 through 27. Again, the nomenclature of the displacement and strain gauges are shown in figures 2 and 3, respectively. The displacement data showed that surfaces of the dome (in the middle of the test section, away from the weld lands) between the equator and third stiffener deflected radially inward, indicating hoop compression. Such behavior was the expected consequence of using the low profile ellipse in the design. The hoop strain gauges at locations C3, C5 and C9 (figs. 20 through 22) also verified this phenomenon. In general, the test displacement data compared very well with the analysis up to about 55 psi, where strain data from back-to-back gauges began to diverge.

By looking at the slopes of the appropriate strain versus pressure curves, one can deduce the stiffness of the structure at a particular location. Observation of the data plots indicated that the hoop compression stiffness of the actual dome was greater than the model hoop compression stiffness. On the other hand, predicted hoop and meridional stiffnesses in the tensile regions of the dome were generally higher than the actual stiffnesses. Some of the discrepancies between the model and the actual dome stiffnesses were due to actual differences between the tensile and compressive Young's moduli not incorporated in the model. Future models will need to account for variations in the moduli, especially in applications that use more anisotropic alloys such as aluminum-lithium for which the tensile and compressive moduli differences are much greater.

Nonlinear bifurcation of back-to-back gauges in the hoop compression region began to occur in the 55 to 60 psi range and became very pronounced at 65 psi and above. After examining the various strain versus pressure plots, significant divergence of back-to-back strains (as seen by a sudden change in the slope of the strain versus pressure curve) occurred at 65 to 66 psi, which was thus determined to be where the onset of first mode buckling occurred. This was also verified by the acoustic emissions data. Additionally, the wavelength measured by laser shearography corresponded to the wavelength produced if there were 64 buckling waves around the dome's circumference. Consequently, the BOSOR analytical prediction of 62 full waves compared well with measured results. The 3–D NASTRAN model analysis predicted a first buckling mode of 69.5 psi (with 81 circumferential waves). The NASTRAN result is remarkably close to the actual first mode buckling pressure considering that the NASTRAN solution was a linear eigenvalue solution. The accuracy of the analytical predictions seems to indicate that a knockdown factor of 0.9 on a linear eigenvalue solution is adequate to predict first mode buckling of this dome. Similar knockdown factors are expected for low-profile elliptical domes of other major-to-minor radius ratios. A nonlinear solution would be required if a more accurate prediction of the circumferential wavelength was required. Such a model should also take into account boundary conditions imposed by weld lands and other circumferential variations in thicknesses which will affect the wavelength.

V. CONCLUSIONS

The BOSOR nonlinear analysis most accurately predicted first mode buckling, with 62 to 65 psig predicted and 65 to 66 psig actual. The NASTRAN linear eigenvalue prediction of 69.5 psig was within 5 to 7 percent of the first buckling mode. ANSYS and NASTRAN stress analysis predictions also accurately indicated that ultimate (biaxial tension) dome failure would occur between the last two load steps analyzed, 72 and 74 psig (72.6 psig actual). Both quantitative and qualitative dome response test data were also provided by acoustic emissions, digital image correlation, and laser shearography non-destructive evaluation techniques.

Based on the close correlation of the predictions versus results achieved with the 2219 aluminum low-profile dome, state-of-the-art analysis tools can be used to accurately predict response and ultimate failure of isotropic low-profile domes loaded under internal pressurization. The next logical step in the CTTP is to use this test as a pathfinder and to expand the analysis versus test correlation data base for low-profile domes to include anisotropic (aluminum-lithium) low-profile dome designs.

REFERENCES

1. Harvey, J.F.: "Theory and Design of Pressure Vessels." Van Nostrand Reinhold, 1980.

2. Bruhn, E.F.: "Missile Structures Analysis and Design." Tri-State Offset Co., 1967.

3. Sisk, D.B., et al: "Cryogenic Tank Technology Program." GDSS-ERR-91-304, December 1991.

4. DeSalvo, G.J., and Gorman, R.W.: "ANSYS Engineering Analysis System User's Manual (Rev. 4.4)." May 1989.

5. Department of Defense: "Military Standardization Handbook—Metallic Materials and Elements for Aerospace Vehicle Structures." MIL-HDBK-5E, June 1987.

6. Hill, E.: "Cryogenic Tank Technology Program Acoustic Emission Report." Q.A. Technologies, 1993.

7. King, T.: "Shearographic Optical NDE of a Subscale Cryogenic Tank Dome." Pratt and Whitney, MET-35298, 1993.

Table 1. Predicted displacements versus pressure.

Pressure (psi)	D1 Pred. (in)	D2 Pred. (in)	D3 Pred. (in)	D4 Pred. (in)	D5 Pred. (in)	D6 Pred. (in)	D7 Pred. (in)	D8 Pred. (in)
0.00E+00	0.00E+00	0.00E+00	0.00E+00	0.00E+00	0.00E+00	0.00E+00	0.00E+00	0.00E+00
3.75E+01	2.80E–02	3.50E–04	–4.28E–02	–4.10E–02	–1.49E–02	9.66E–03	5.89E–02	6.06E–02
5.00E+01	3.74E–02	4.71E–04	–5.71E–02	–5.48E–02	–1.98E–02	1.12E–02	7.90E–02	7.84E–02
5.50E+01	4.16E–02	5.20E–04	–6.35E–02	–6.21E–02	–2.56E–02	2.75E–03	8.78E–02	8.90E–02
6.00E+01	4.52E–02	5.00E–04	–7.33E–02	–8.60E–02	–4.01E–02	–4.20E–03	1.04E–01	1.18E–01
6.50E+01	4.89E–02	4.10E–04	–9.20E–02	–1.26E–01	–5.43E–02	–6.87E–03	1.27E–01	1.51E–01
7.00E+01	5.30E–02	2.60E–04	–1.13E–01	–1.73E–01	–8.24E–02	–2.48E–02	1.52E–01	1.98E–01
7.20E+01	5.47E–02	1.60E–04	–1.25E–01	–2.01E–01	–1.04E–01	–3.61E–02	1.70E–01	2.29E–01
Pressure (psi)	D9 Pred. (in)	D10 Pred. (in)	D11 Pred. (in)	D12 Pred. (in)	D13 Pred. (in)	D14 Pred. (in)	D15 Pred. (in)	D16 Pred. (in)
0.00E+00	0.00E+00	0.00E+00	0.00E+00	0.00E+00	0.00E+00	0.00E+00	0.00E+00	0.00E+00
3.75E+01	9.29E–02	1.03E–01	1.12E–01	1.16E–01	1.16E–01	1.09E–01	1.01E–01	9.75E–02
5.00E+01	1.25E–01	1.40E–01	1.51E–01	1.56E–01	1.57E–01	1.48E–01	1.36E–01	1.32E–01
5.50E+01	1.46E–01	1.63E–01	1.75E–01	1.82E–01	1.82E–01	1.72E–01	1.64E–01	1.55E–01
6.00E+01	1.89E–01	2.09E–01	2.24E–01	2.31E–01	2.32E–01	2.21E–01	2.07E–01	2.03E–01
6.50E+01	2.47E–01	2.72E–01	2.89E–01	2.98E–01	2.99E–01	2.88E–01	2.73E–01	2.68E–01
7.00E+01	3.31E–01	3.60E–01	3.80E–01	3.91E–01	3.92E–01	3.81E–01	3.65E–01	3.60E–01
7.20E+01	3.80E–01	4.12E–01	4.34E–01	4.45E–01	4.47E–01	4.36E–01	4.20E–01	4.15E–01

Table 2. Actual displacements versus pressure.

Pressure (psi)	D1 Act. (in)	D2 Act. (in)	D3 Act. (in)	D4 Act. (in)	D5 Act. (in)	D6 Act. (in)	D7 Act. (in)	D8 Act. (in)
0.00E+00	0.00E+00	0.00E+00	0.00E+00	0.00E+00	0.00E+00	0.00E+00	0.00E+00	0.00E+00
3.75E+01	-2.04E-02	1.97E-02	-2.97E-02	-2.20E-02	-2.21E-03	2.47E-02	5.63E-02	7.12E-02
5.00E+01	-2.78E-02	2.83E-02	-3.82E-02	-2.86E-02	-1.64E-03	3.53E-02	7.77E-02	9.90E-02
5.50E+01	-3.14E-02	3.24E-02	-4.27E-02	-3.31E-02	-1.96E-03	4.05E-02	8.96E-02	1.15E-01
6.00E+01	-3.59E-02	3.73E-02	-4.89E-02	-4.05E-02	-4.28E-03	4.69E-02	1.06E-01	1.37E-01
6.50E+01	-4.20E-02	4.10E-02	-6.10E-02	-5.60E-02	-1.10E-02	5.30E-02	1.35E-01	1.65E-01
7.00E+01	-5.20E-02	4.20E-02	-8.50E-02	-9.00E-02	-3.10E-02	5.30E-02	1.58E-01	2.00E-01
7.20E+01	-5.50E-02	4.50E-02	-9.10E-02	-9.60E-02	-3.30E-02	5.70E-02	1.67E-01	2.14E-01
Pressure (psi)	D9 Act. (in)	D10 Act. (in)	D11 Act. (in)	D12 Act. (in)	D13 Act. (in)	D14 Act. (in)	D15 Act. (in)	D16 Act. (in)
0.00E+00	0.00E+00	0.00E+00	0.00E+00	0.00E+00	0.00E+00	0.00E+00	0.00E+00	0.00E+00
3.75E+01	8.99E-02	1.01E-01	1.07E-01	1.12E-01	1.18E-01	1.20E-01	1.17E-01	1.10E-01
5.00E+01	1.24E-01	1.38E-01	1.46E-01	1.55E-01	1.62E-01	1.64E-01	1.61E-01	1.53E-01
5.50E+01	1.43E-01	1.58E-01	1.67E-01	1.77E-01	1.86E-01	1.89E-01	1.85E-01	1.78E-01
6.00E+01	1.70E-01	1.86E-01	1.98E-01	2.10E-01	2.20E-01	2.24E-01	2.20E-01	2.14E-01
6.50E+01	2.04E-01	2.22E-01	2.38E-01	2.53E-01	2.64E-01	2.68E-01	2.64E-01	2.60E-01
7.00E+01	2.48E-01	2.67E-01	2.88E-01	3.07E-01	3.20E-01	3.24E-01	3.19E-01	3.20E-01
7.20E+01	2.66E-01	2.70E-01	3.10E-01	3.30E-01	3.45E-01	3.49E-01	3.43E-01	3.47E-01

Table 3. Predicted strains versus pressure.

Pressure (psi)	C3 Inside Hoop	C5 Inside Hoop	C9 Inside Hoop	C14 Inside Hoop	C3 Inside Merid.	C5 Inside Merid.	C9 Inside Merid.	C14 Inside Merid.
0.00E+00	0.00E+00	0.00E+00	0.00E+00	0.00E+00	0.00E+00	0.00E+00	0.00E+00	0.00E+00
3.75E+01	2.80E–02	3.50E–04	–4.28E–02	–4.10E–02	–1.49E–02	9.66E–03	5.89E–02	6.06E–02
5.00E+01	3.74E–02	4.71E–04	–5.71E–02	–5.48E–02	–1.98E–02	1.12E–02	7.90E–02	7.84E–02
5.50E+01	4.16E–02	5.20E–04	–6.35E–02	–6.21E–02	–2.56E–02	2.75E–03	8.78E–02	8.90E–02
6.00E+01	4.52E–02	5.00E–04	–7.33E–02	–8.60E–02	–4.01E–02	–4.20E–03	1.04E–01	1.18E–01
6.50E+01	4.89E–02	4.10E–04	–9.20E–02	–1.26E–01	–5.43E–02	–6.87E–03	1.27E–01	1.51E–01
7.00E+01	5.30E–02	2.60E–04	–1.13E–01	–1.73E–01	–8.24E–02	–2.48E–02	1.52E–01	1.98E–01
7.20E+01	5.47E–02	1.60E–04	–1.25E–01	–2.01E–01	–1.04E–01	–3.61E–02	1.70E–01	2.29E–01
Pressure (psi)	C3 Outside Hoop	C5 Outside Hoop	C9 Outside Hoop	C14 Outside Hoop	C3 Outside Merid.	C5 Outside Merid.	C9 Outside Merid.	C14 Outside Merid.
0.00E+00	0.00E+00	0.00E+00	0.00E+00	0.00E+00	0.00E+00	0.00E+00	0.00E+00	0.00E+00
3.75E+01	9.29E–02	1.03E–01	1.12E–01	1.16E–01	1.16E–01	1.09E–01	1.01E–01	9.75E–02
5.00E+01	1.25E–01	1.40E–01	1.51E–01	1.56E–01	1.57E–01	1.48E–01	1.36E–01	1.32E–01
5.50E+01	1.46E–01	1.63E–01	1.75E–01	1.82E–01	1.82E–01	1.72E–01	1.64E–01	1.55E–01
6.00E+01	1.89E–01	2.09E–01	2.24E–01	2.31E–01	2.32E–01	2.21E–01	2.07E–01	2.03E–01
6.50E+01	2.47E–01	2.72E–01	2.89E–01	2.98E–01	2.99E–01	2.88E–01	2.73E–01	2.68E–01
7.00E+01	3.31E–01	3.60E–01	3.80E–01	3.91E–01	3.92E–01	3.81E–01	3.65E–01	3.60E–01
7.20E+01	3.80E–01	4.12E–01	4.34E–01	4.45E–01	4.47E–01	4.36E–01	4.20E–01	4.15E–01

Table 4. Actual strain versus pressure.

Pressure (psi)	C3 Inside Hoop	C5 Inside Hoop	C9 Inside Hoop	C14 Inside Hoop	C3 Inside Merid.	C5 Inside Merid.	C9 Inside Merid.	C14 Inside Merid.
0.00E+00	0.00E+00	0.00E+00	0.00E+00	0.00E+00	0.00E+00	0.00E+00	0.00E+00	0.00E+00
1.50E+01	–6.96E+02	–4.02E+02	–3.87E+02	–1.84E+02	7.37E+02	6.75E+02	1.01E+03	1.11E+03
3.00E+01	–1.20E+03	–8.77E+02	–7.02E+02	–3.15E+02	1.38E+03	1.35E+03	1.90E+03	2.09E+03
3.75E+01	–1.45E+03	–1.08E+03	–8.58E+02	–3.70E+02	1.70E+03	1.71E+03	2.35E+03	2.60E+03
5.00E+01	–189E+03	–1.58E+03	–1.17E+03	–4.99E+02	2.28E+03	2.43E+03	3.20E+03	3.77E+03
5.50E+01	–2.09E+03	–1.79E+03	–1.33E+03	–5.75E+02	2.57E+03	2.79E+03	3.71E+03	5.02E+03
6.00E+01	–2.32E+03	–2.04E+03	–1.57E+03	–7.56E+02	2.94E+03	3.25E+03	4.49E+03	7.65E+03
6.50E+01	–2.36E+03	–1.84E+03	–1.83E+03	2.02E+02	3.46E+03	3.80E+03	5.87E+03	3.84E+03
7.00E+01	–1.25E+03	–1.32E+03	–2.39E+03	3.54E+02	3.88E+03	4.02E+03	8.22E+03	3.64E+03
7.20E+01	–5.26E+02	–8.57E+02	–2.63E+03	4.37E+02	4.12E+03	4.11E+03	9.33E-03	3.71E+03
Pressure (psi)	C3 Outside Hoop	C5 Outside Hoop	C9 Outside Hoop	C14 Outside Hoop	C3 Outside Merid.	C5 Outside Merid.	C9 Outside Merid.	C14 Outside Merid.
0.00E+00	0.00E+00	0.00E+00	0.00E+00	0.00E+00	0.00E+00	0.00E+00	0.00E+00	0.00E+00
1.50E+01	–6.96E+02	–6.01E+02	–4.21E+02	–1.68E+02	6.53E+02	1.05E+03	1.05E+03	1.24E+03
3.00E+01	–1.20E+03	–1.09E+03	–7.61E+02	–2.75E+02	1.20E+03	1.93E+03	1.98E+03	2.30E+03
3.75E+01	–1.45E+03	–1.33E+03	–9.24E+02	–3.28E+02	1.49E+03	2.36E+03	2.45E+03	2.84E+03
5.00E+01	–1.89E+03	–1.77E+03	–1.26E+03	–4.50E+02	2.00E+03	3.20E+03	3.34E+03	4.04E+03
5.50E+01	–2.09E+03	–1.98E+03	–1.44E+03	–5.42E+02	2.24E+03	3.64E+03	3.87E+03	4.94E+03
6.00E+01	–2.32E+03	–2.22E+03	–1.71E+03	–7.01E+02	2.53E+03	4.22E+03	4.74E+03	6.86E+03
6.50E+01	–2.36E+03	–2.46E+03	–2.08E+03	–8.70E+02	2.86E+03	5.02E+03	6.28E+03	1.05E+04
7.00E+01	–1.24E+03	–2.98E+03	–2.79E+03	–1.01E+03	2.26E+03	6.72E+03	8.84E+03	7.14E+03
7.20E+01	–5.26E+02	–3.41E+03	–3.18E+03	–4.60E+02	1.96E+03	7.63E+03	1.00E+04	3.15E+03

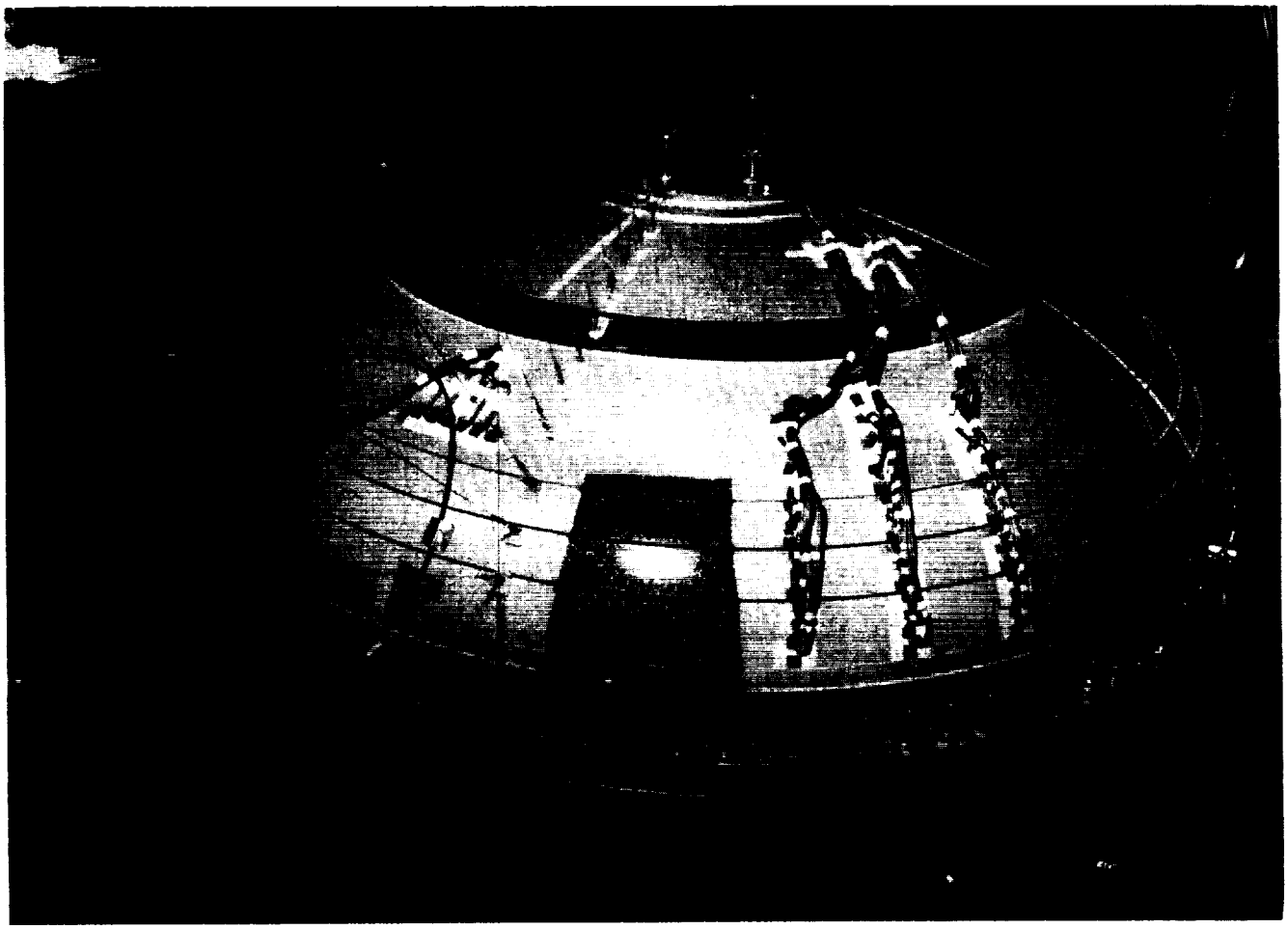

Figure 1. 2219 aluminum low-profile dome test configuration.

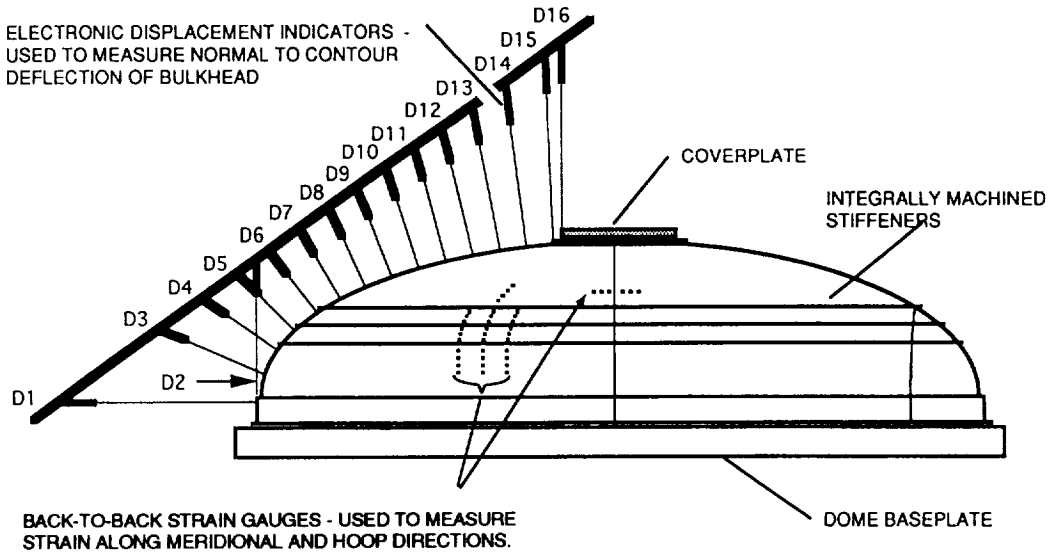

Figure 2. Dome displacement gauge diagram.

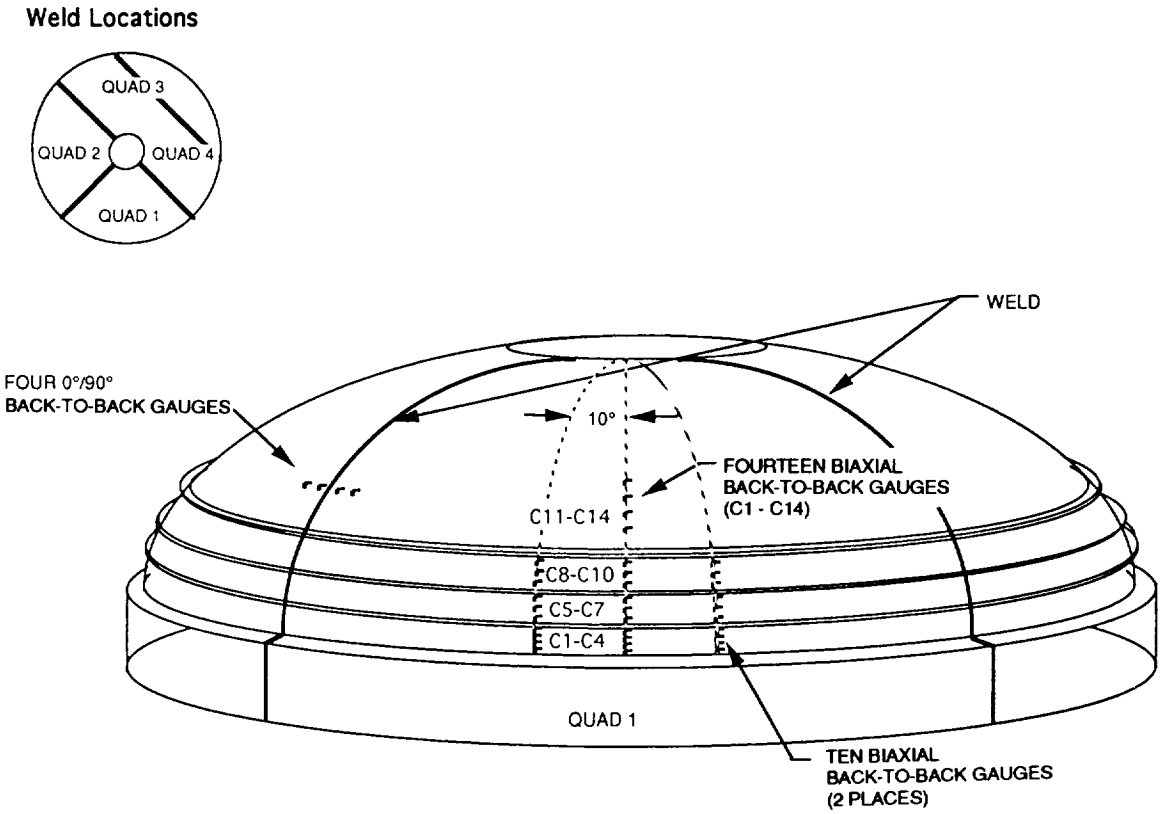

Figure 3. Dome strain gauge diagram.

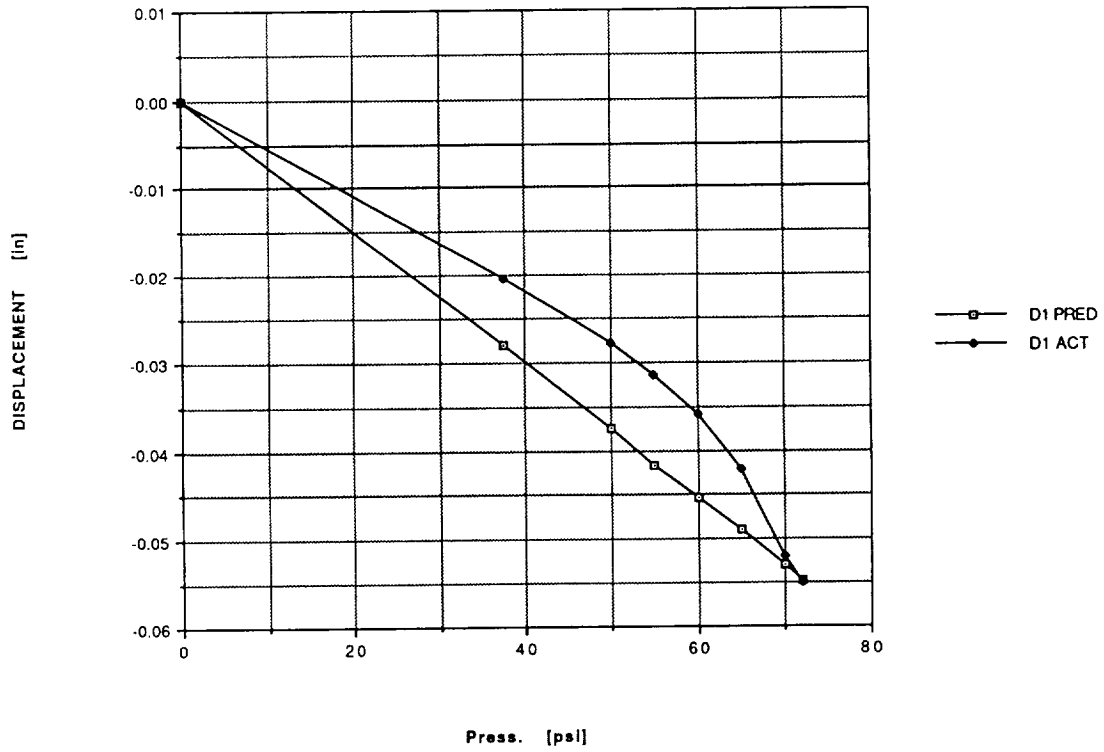

Figure 4. Predicted and actual displacements versus pressure, gauge D1.

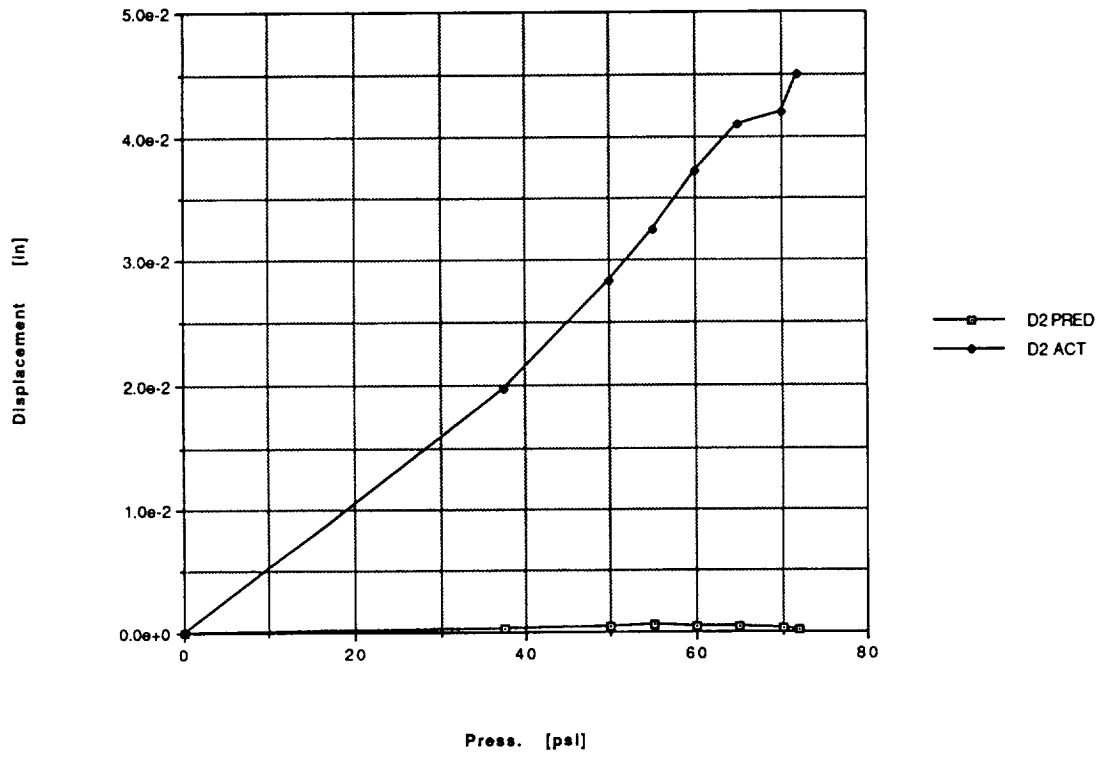

Figure 5. Predicted and actual displacements versus pressure, gauge D2.

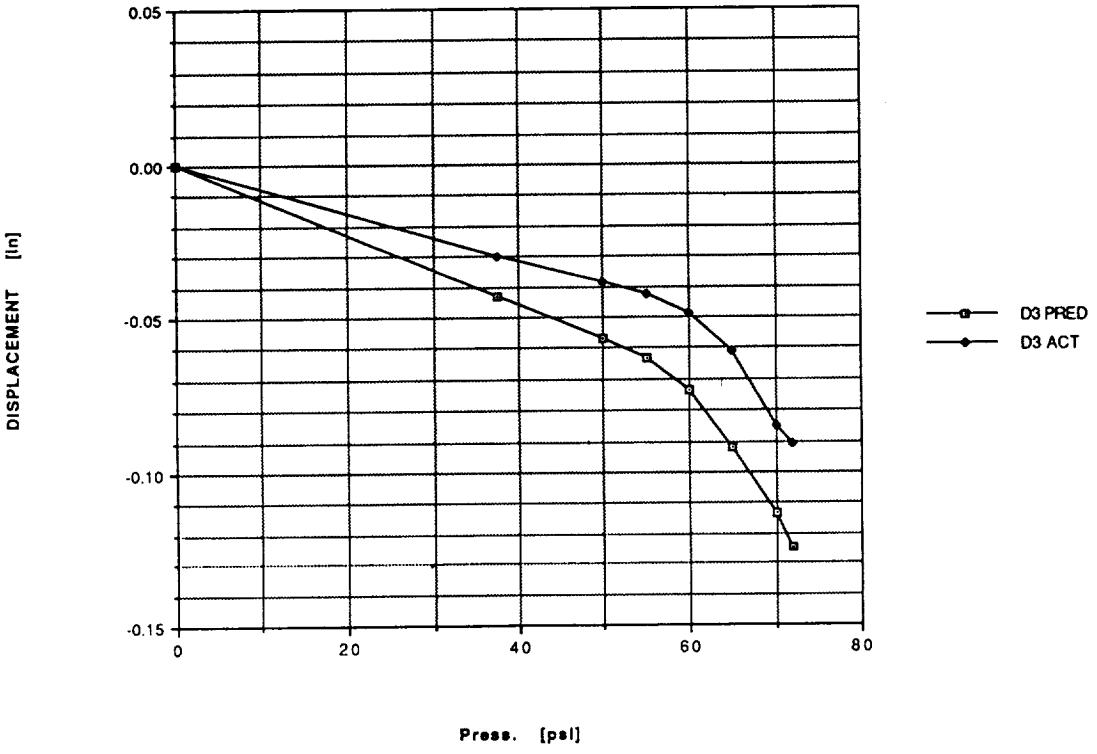

Figure 6. Predicted and actual displacements versus pressure, gauge D3.

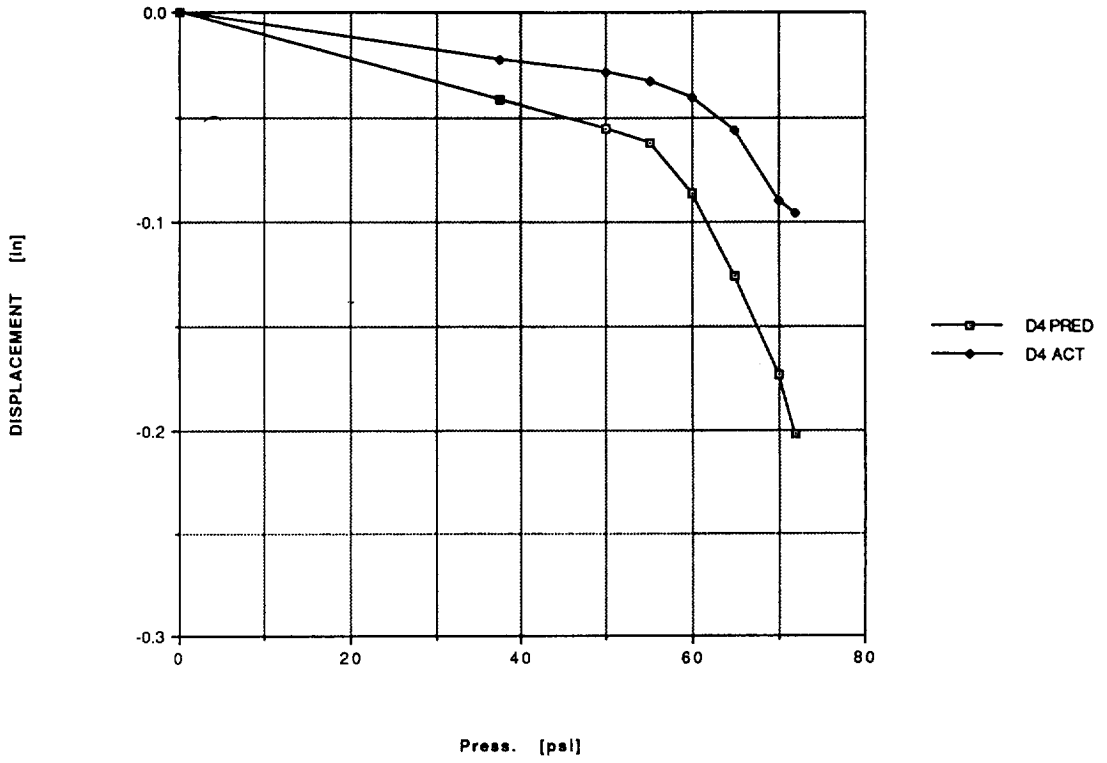

Figure 7. Predicted and actual displacements versus pressure, gauge D4.

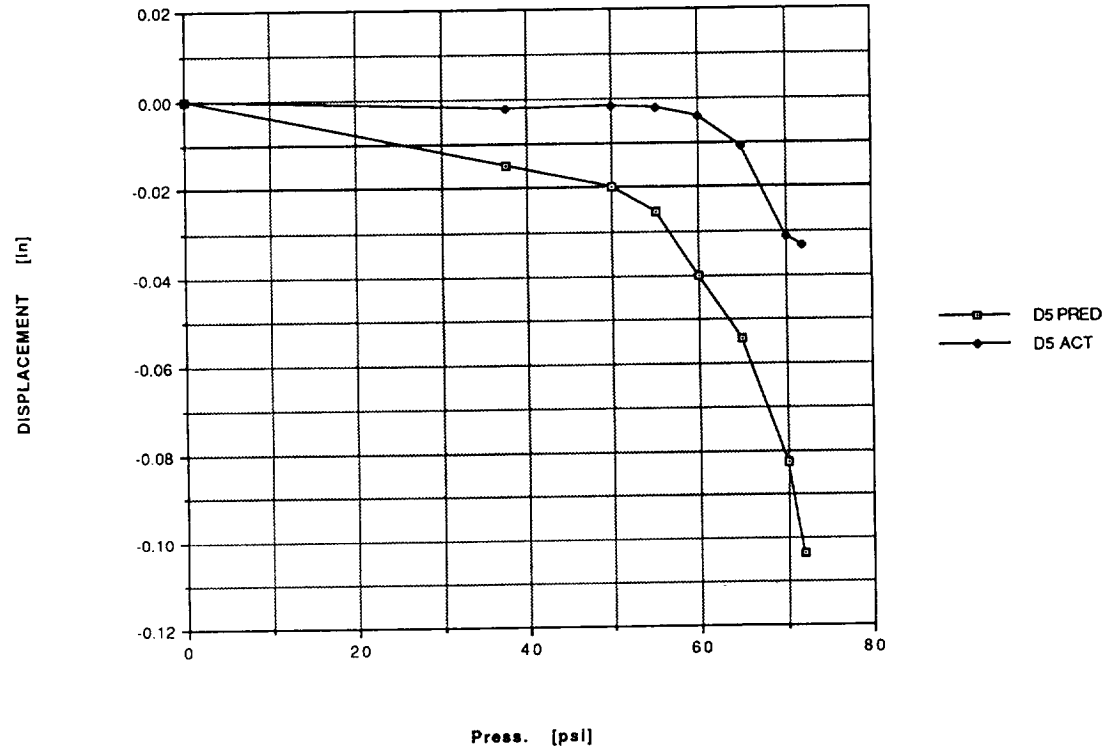

Figure 8. Predicted and actual displacements versus pressure, gauge D5.

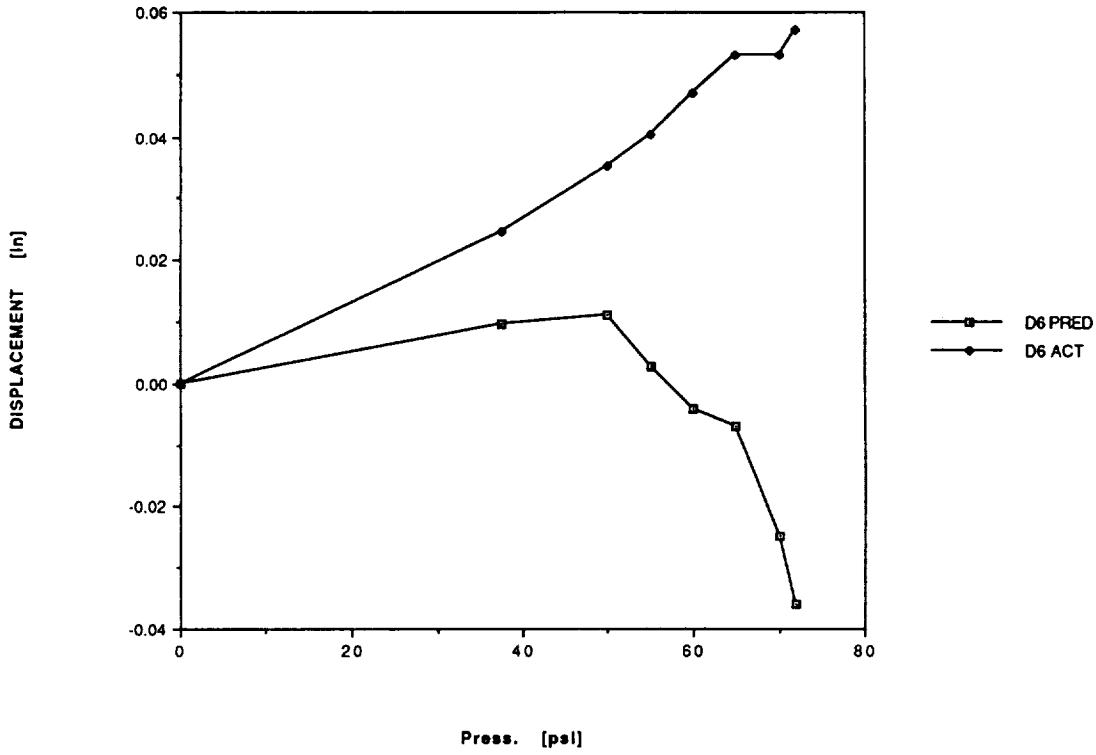

Figure 9. Predicted and actual displacements versus pressure, gauge D6.

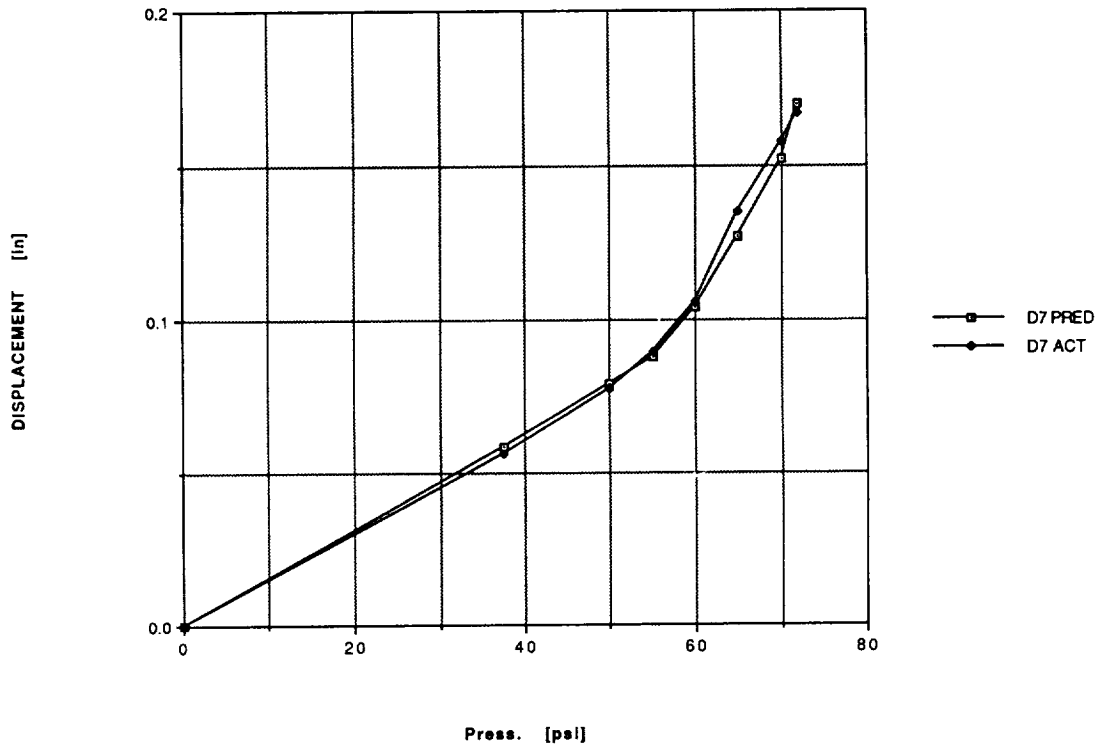

Figure 10. Predicted and actual displacements versus pressure, gauge D7.

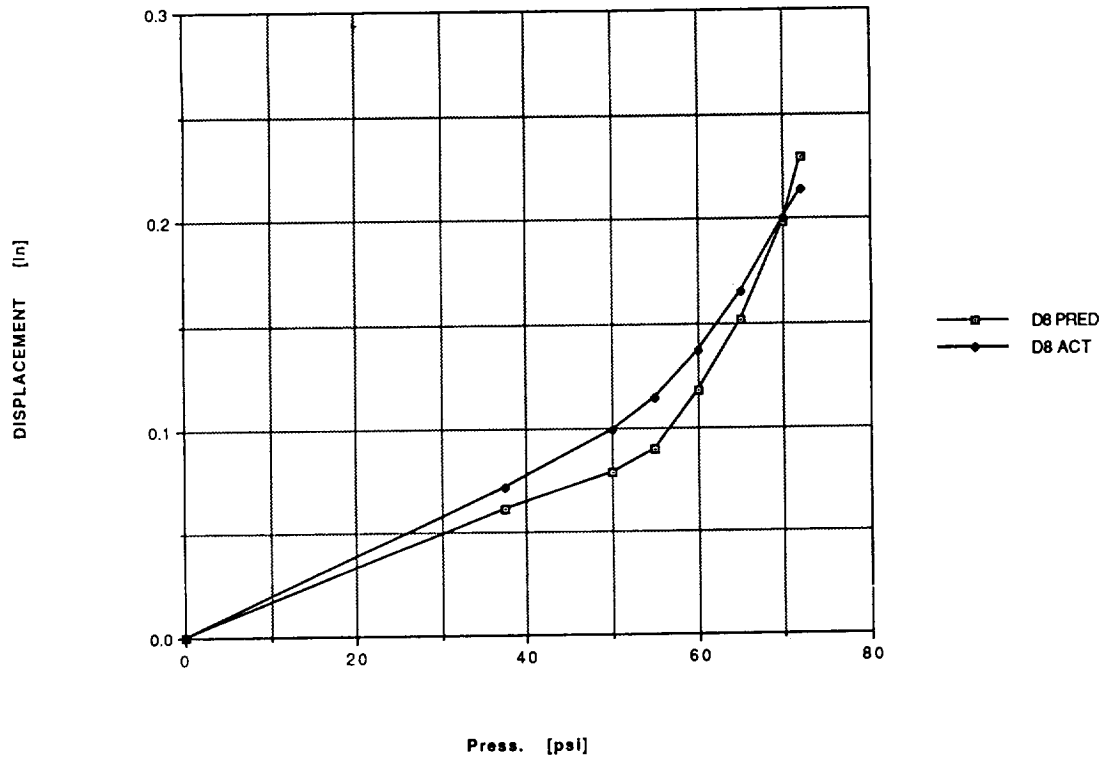

Figure 11. Predicted and actual displacements versus pressure, gauge D8.

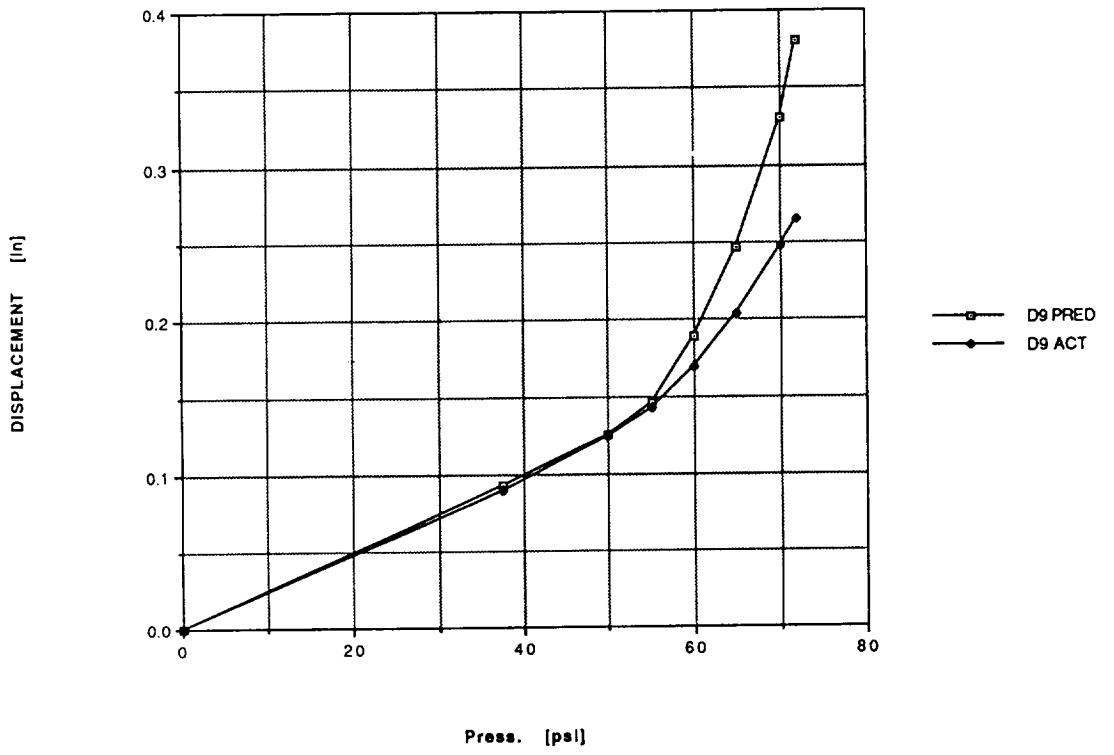

Figure 12. Predicted and actual displacements versus pressure, gauge D9.

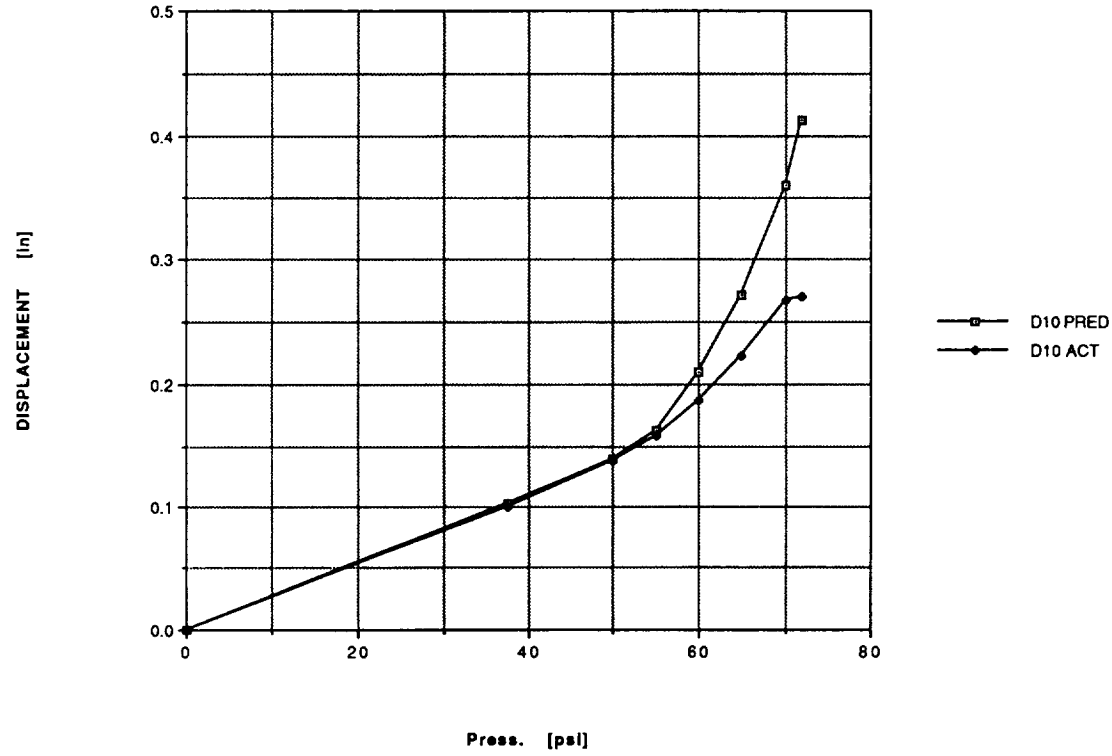

Figure 13. Predicted and actual displacements versus pressure, gauge D10.

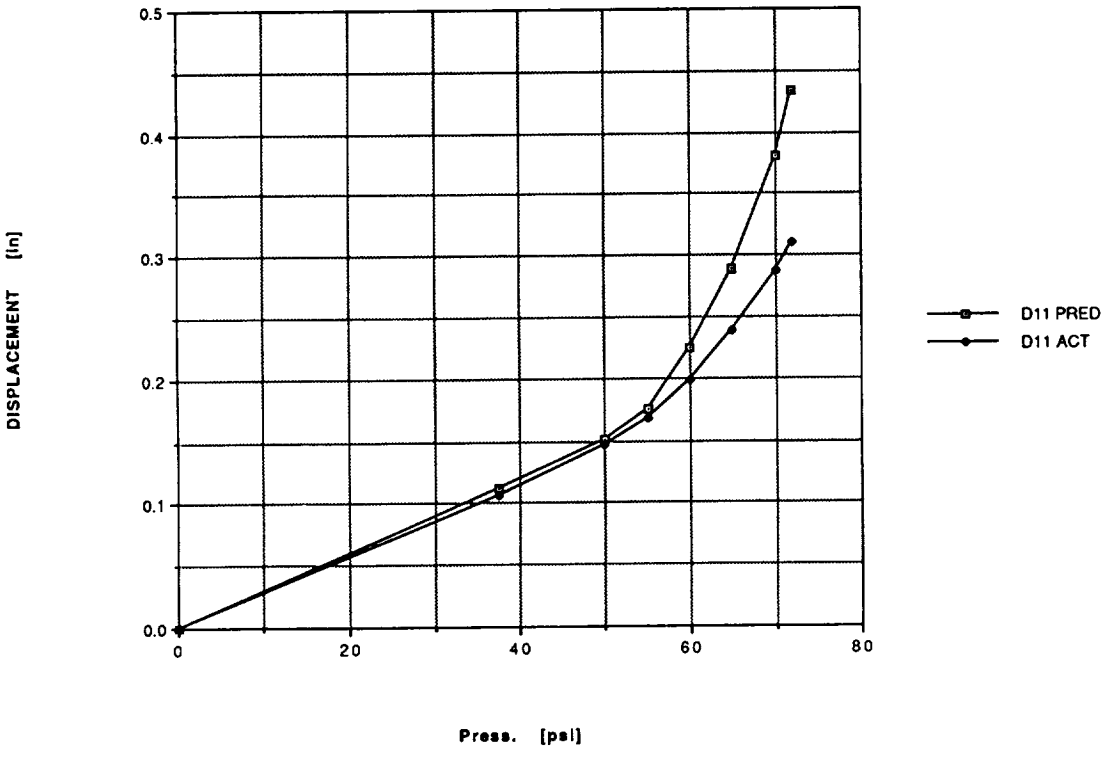

Figure 14. Predicted and actual displacements versus pressure, gauge D11.

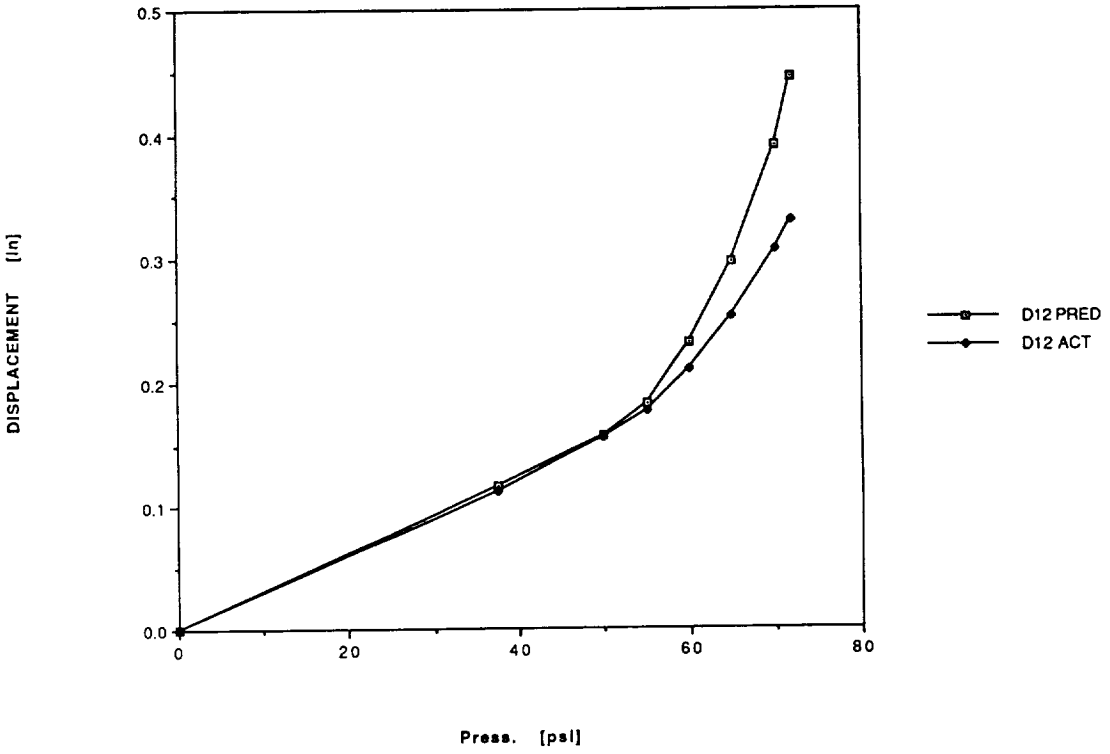

Figure 15. Predicted and actual displacements versus pressure, gauge D12.

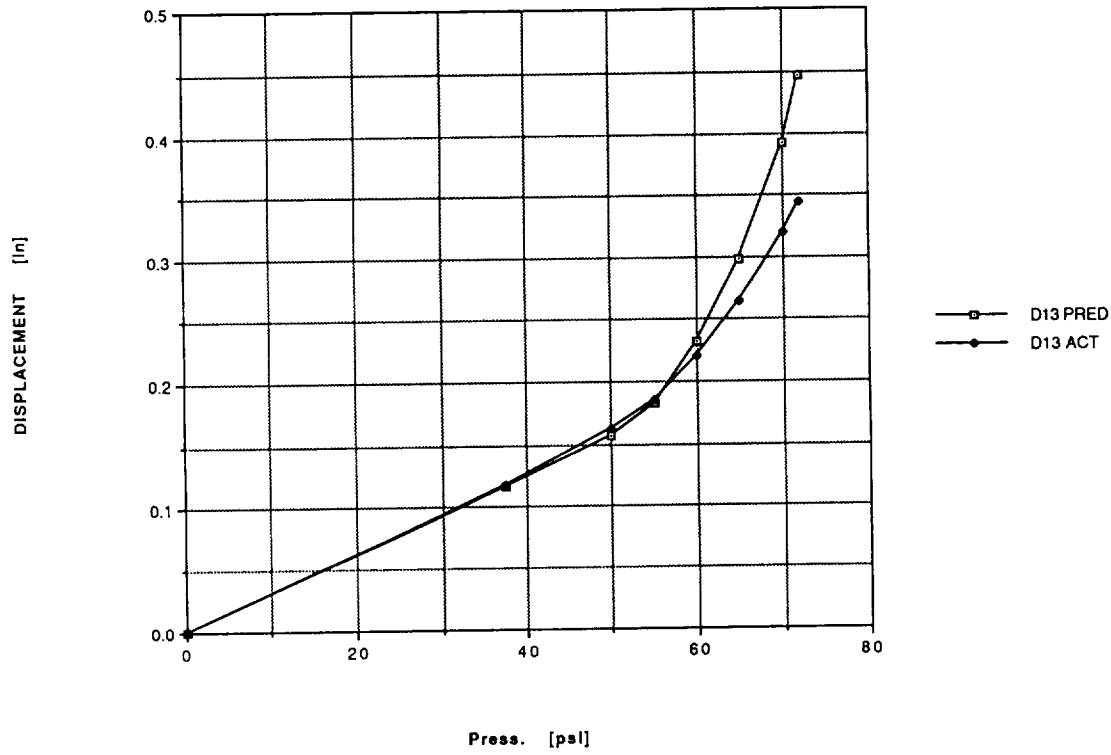

Figure 16. Predicted and actual displacements versus pressure, gauge D13.

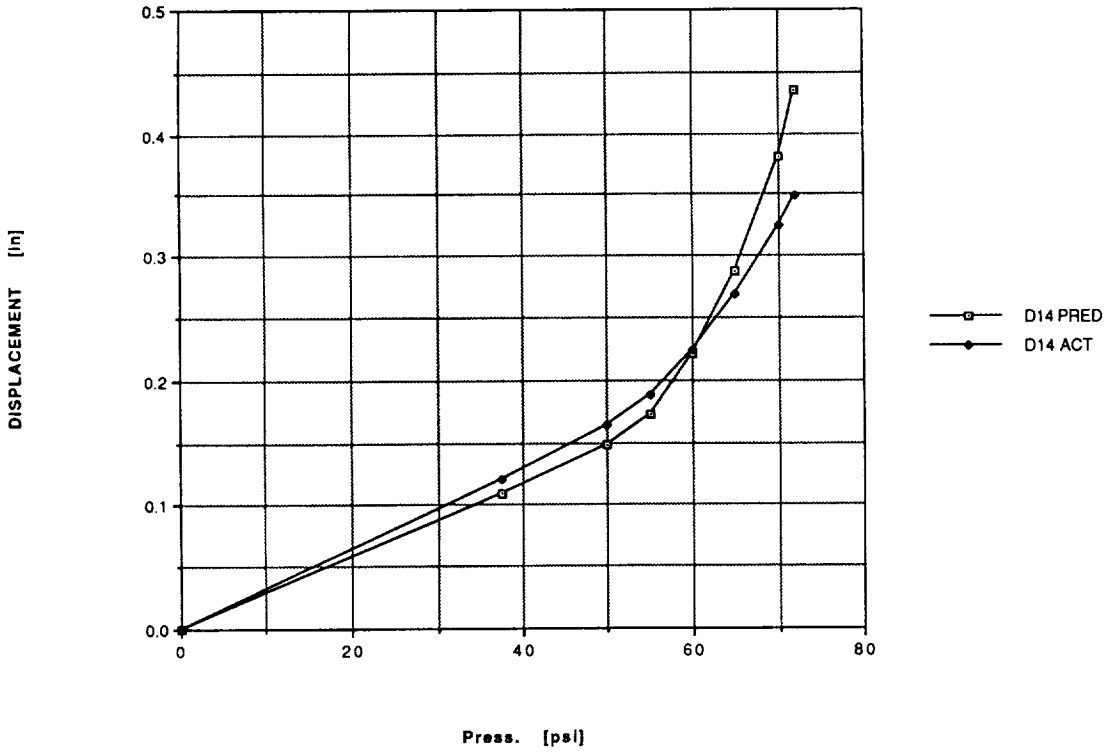

Figure 17. Predicted and actual displacements versus pressure, gauge D14.

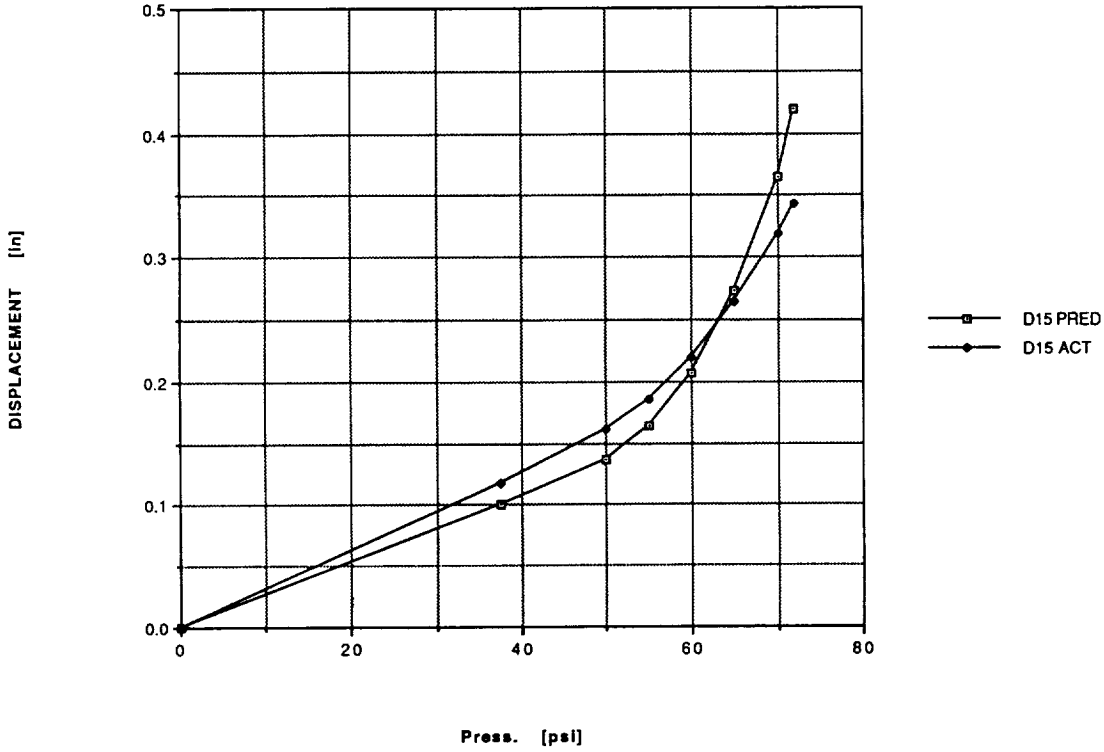

Figure 18. Predicted and actual displacements versus pressure, gauge D15.

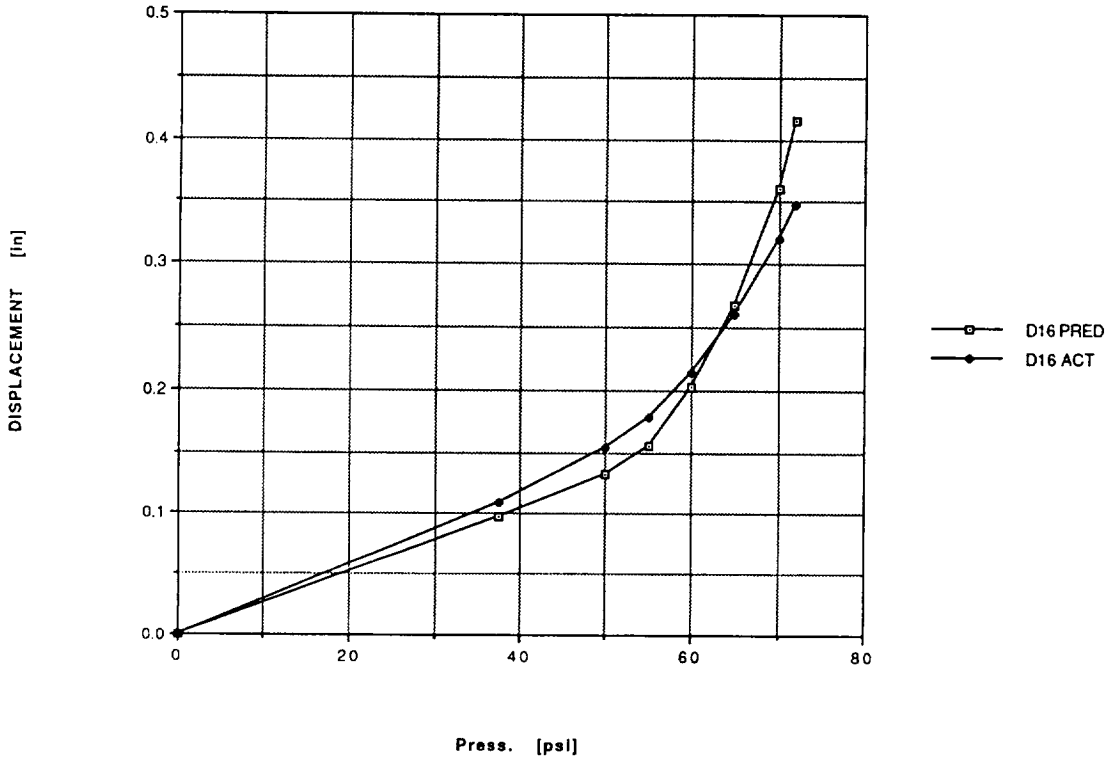

Figure 19. Predicted and actual displacements versus pressure, gauge D16.

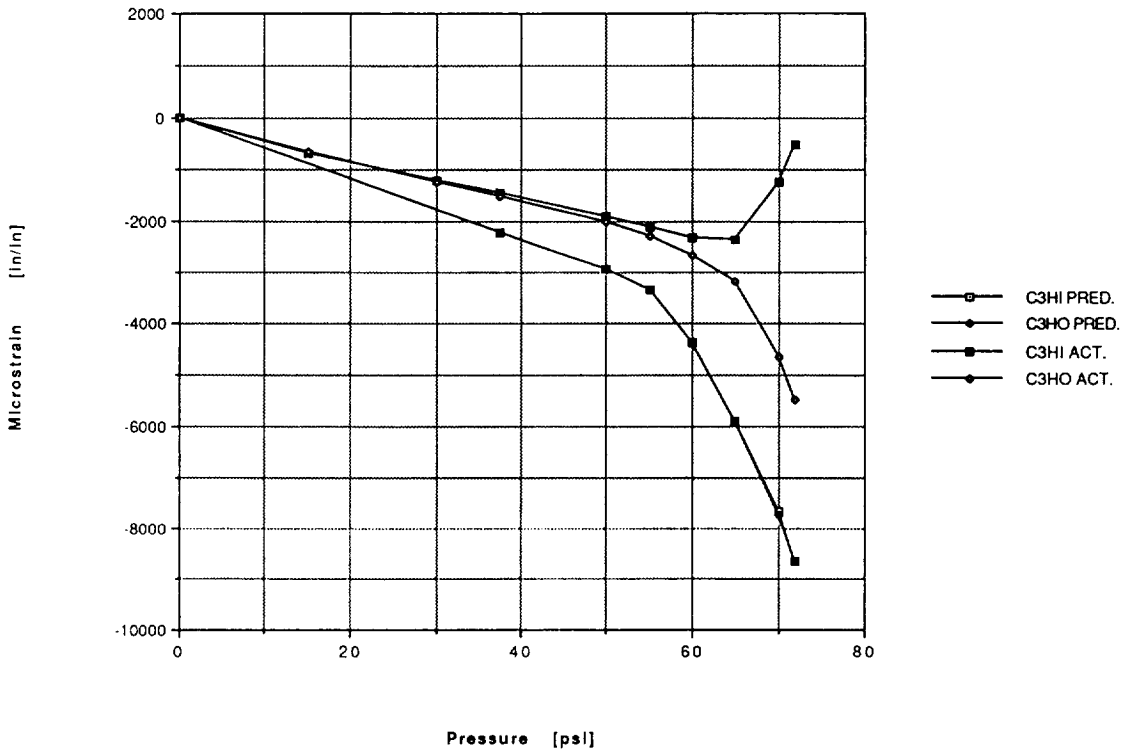

Figure 20. Predicted and actual strains versus pressure, C3 hoop gauges.

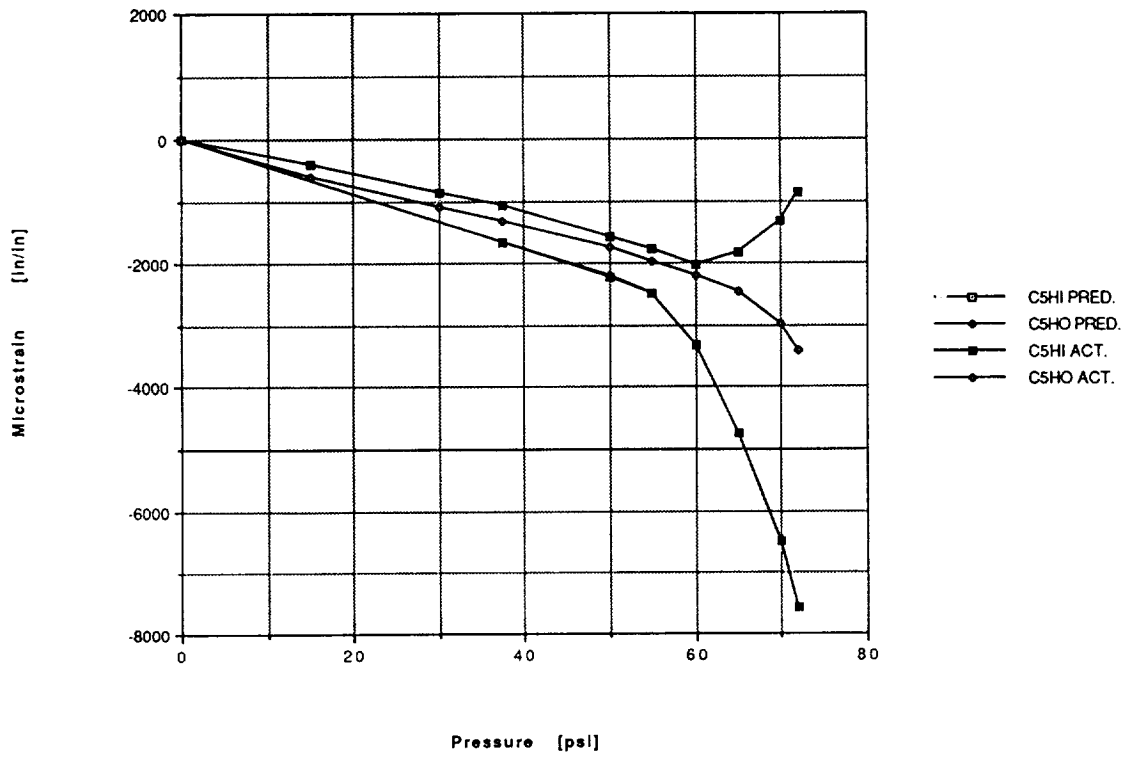

Figure 21. Predicted and actual strains versus pressure, C5 hoop gauges.

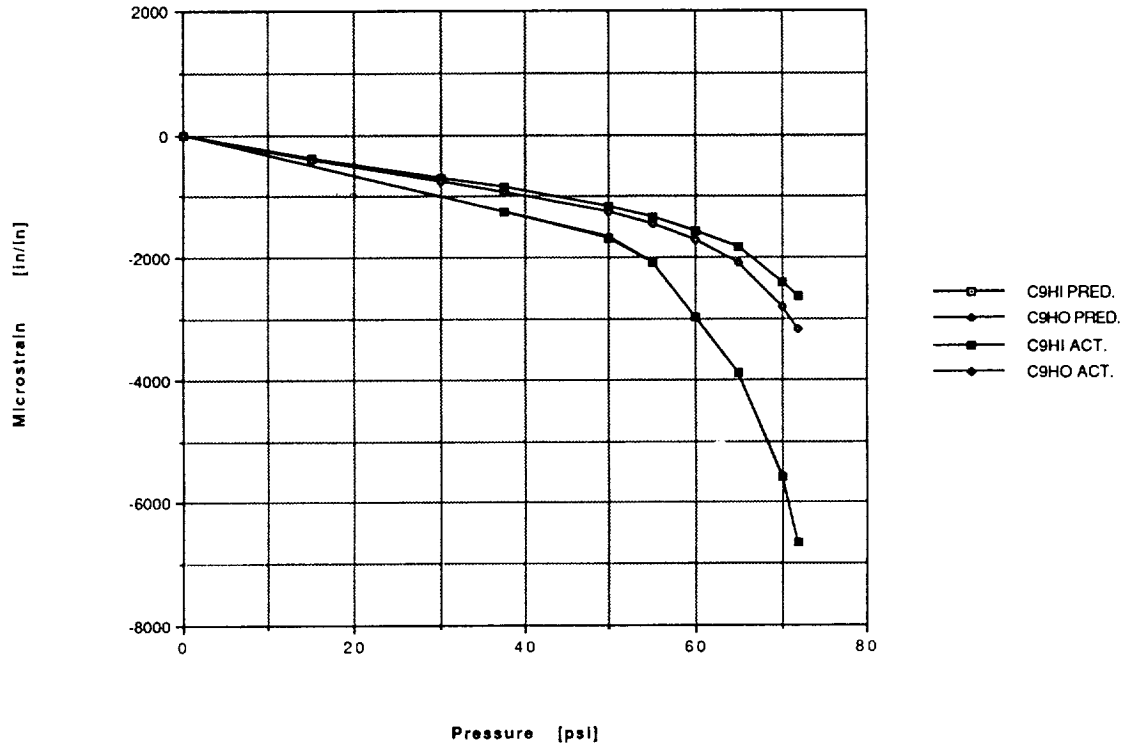

Figure 22. Predicted and actual strains versus pressure, C9 hoop gauges.

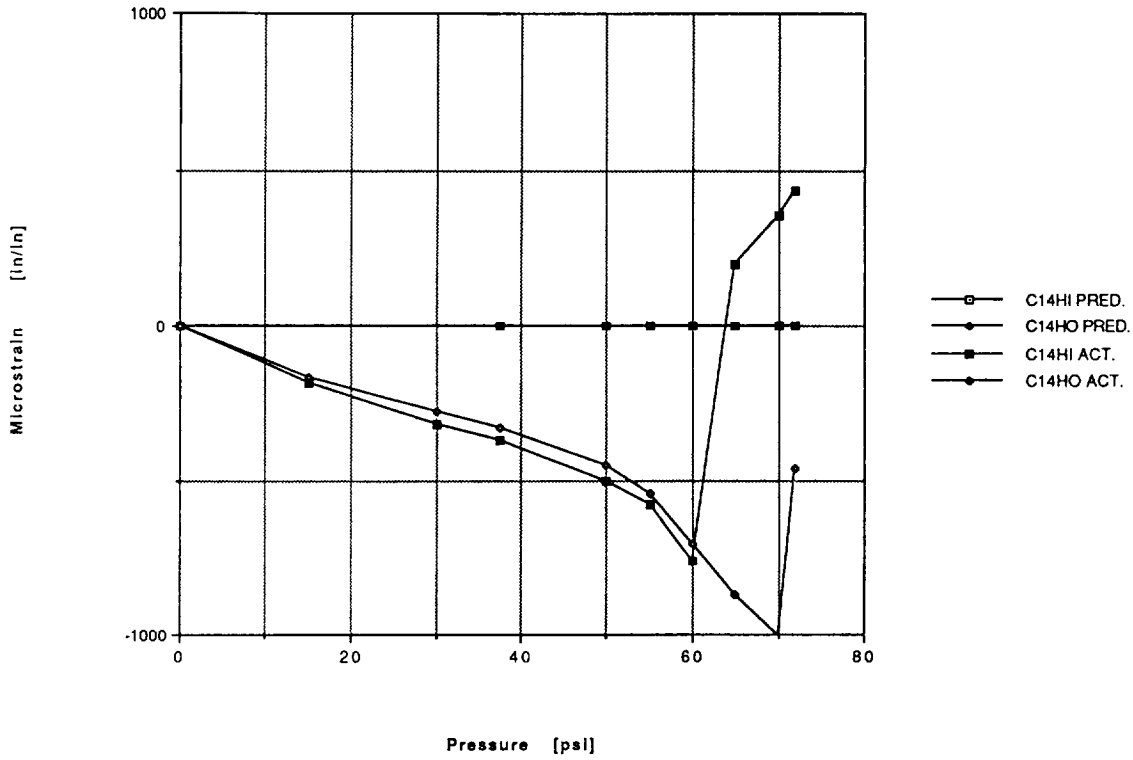

Figure 23. Predicted and actual strains versus pressure, C14 hoop gauges.

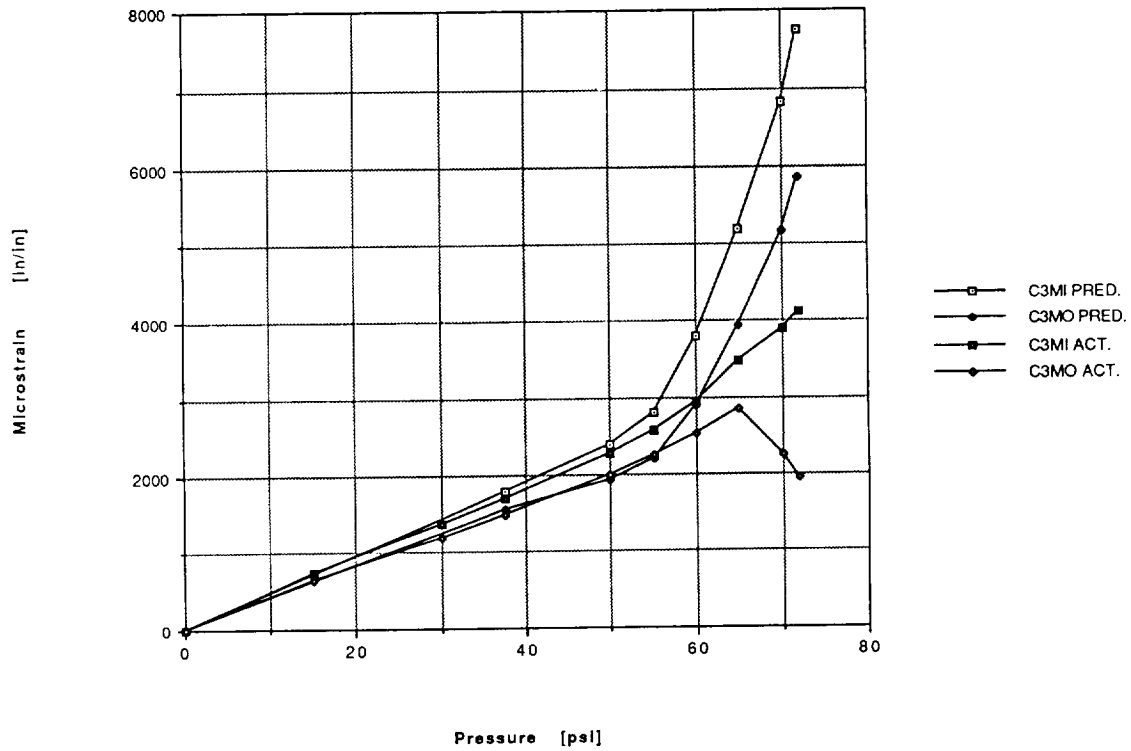

Figure 24. Predicted and actual strains versus pressure, C3 meridional gauges.

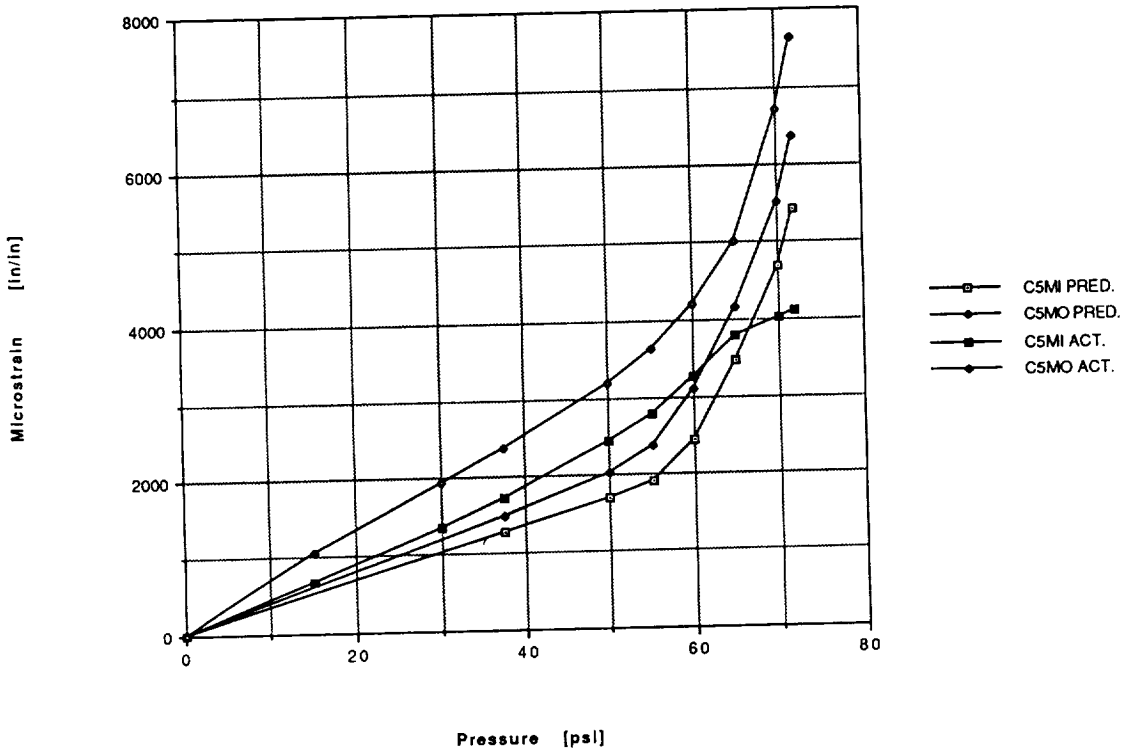

Figure 25. Predicted and actual strains versus pressure, C5 meridional gauges.

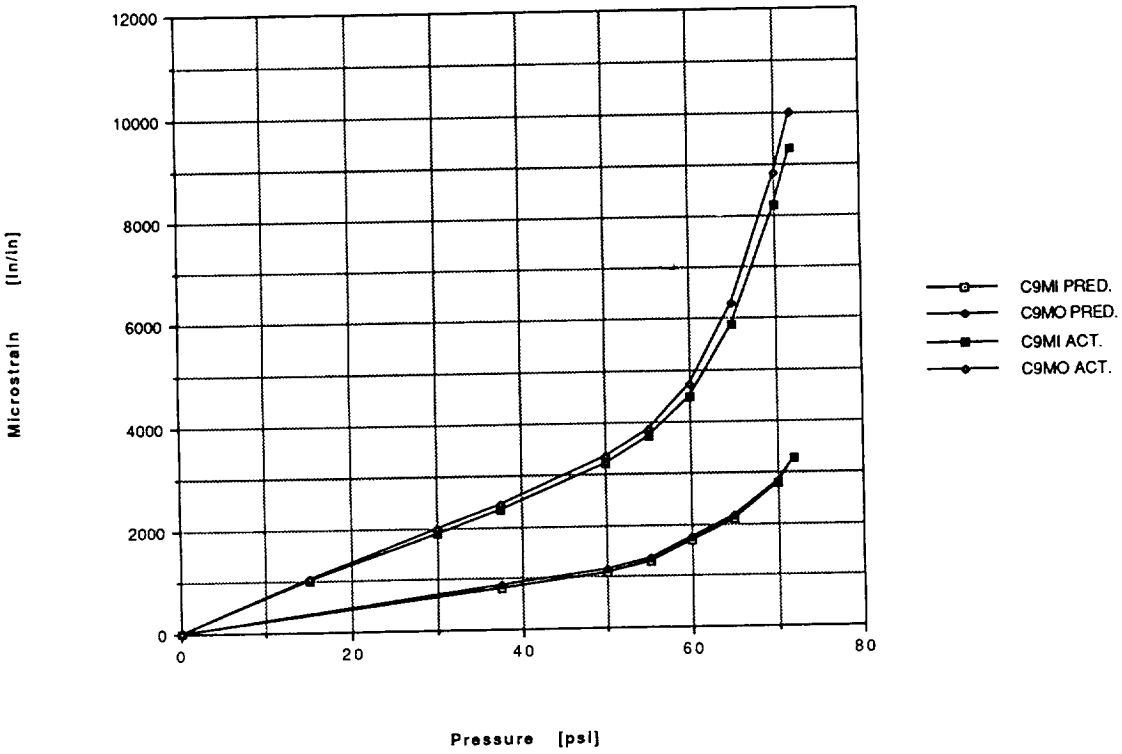

Figure 26. Predicted and actual strains versus pressure, C9 meridional gauges.

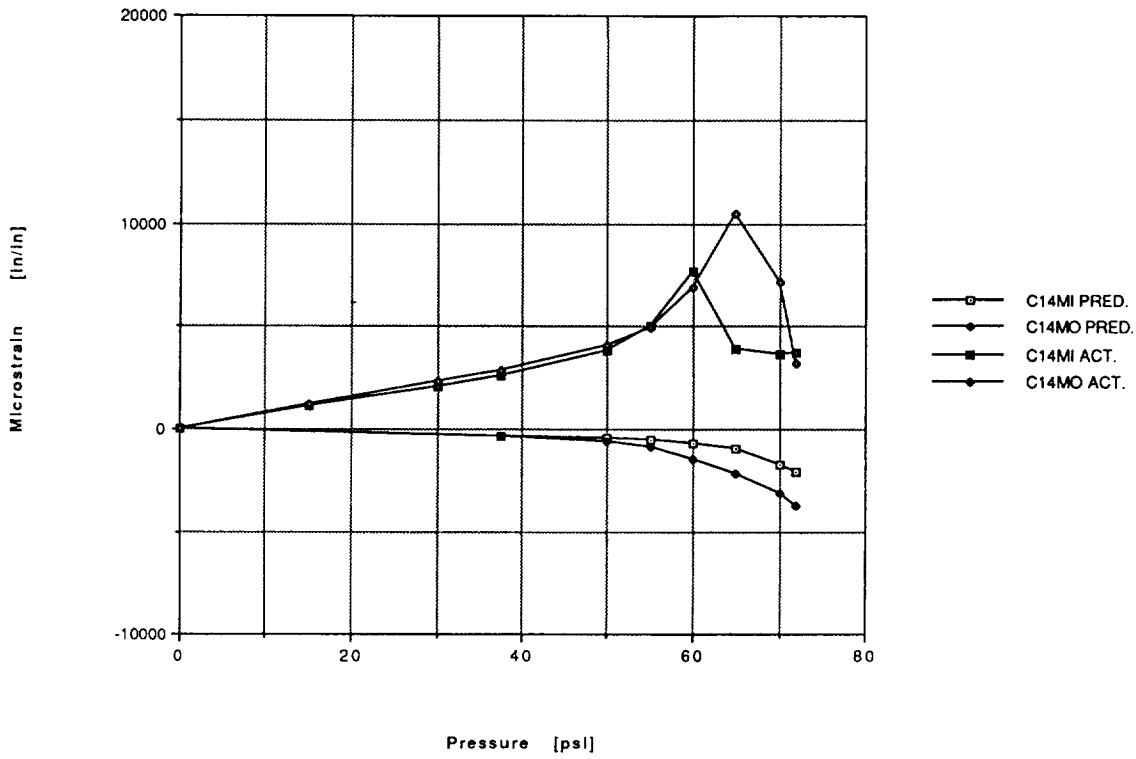

Figure 27. Predicted and actual strains versus pressure, C14 meridional gauges.

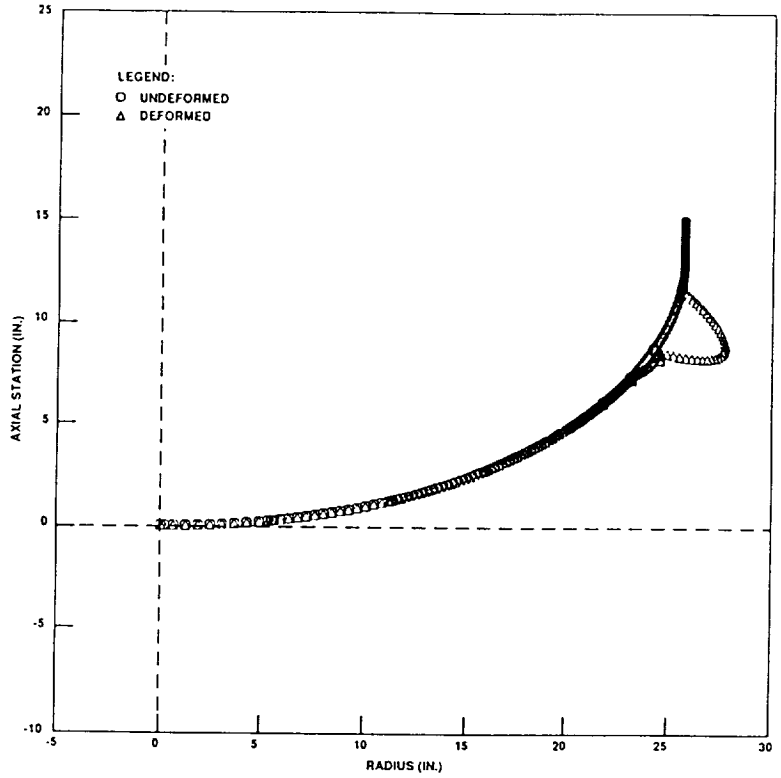

Figure 28. General Dynamics 2–D BOSOR5 model.

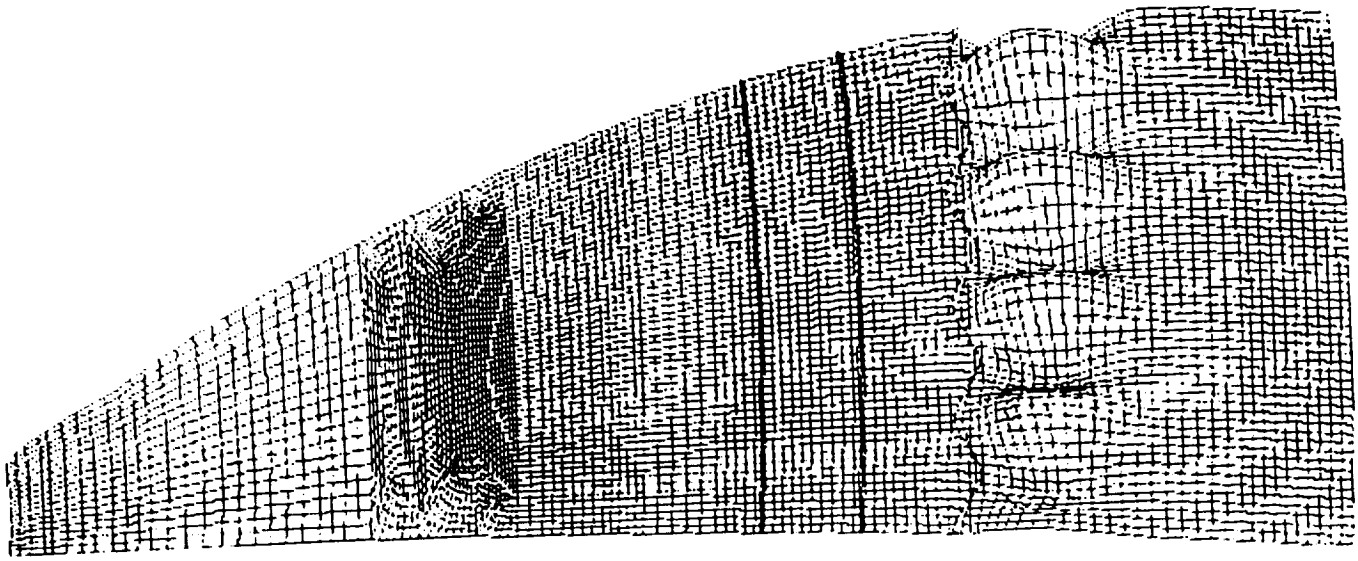

Figure 29. MSFC NASTRAN finite element model showing first mode buckling at 69.5 psi.

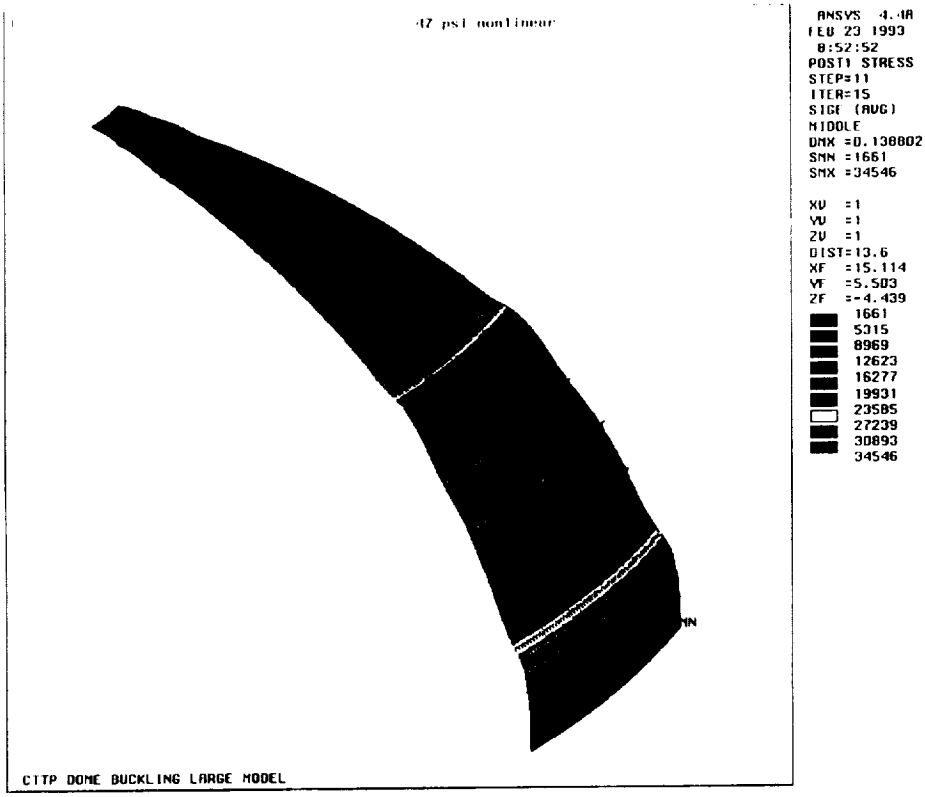

Figure 30. MSFC ANSYS 3–D finite element model.

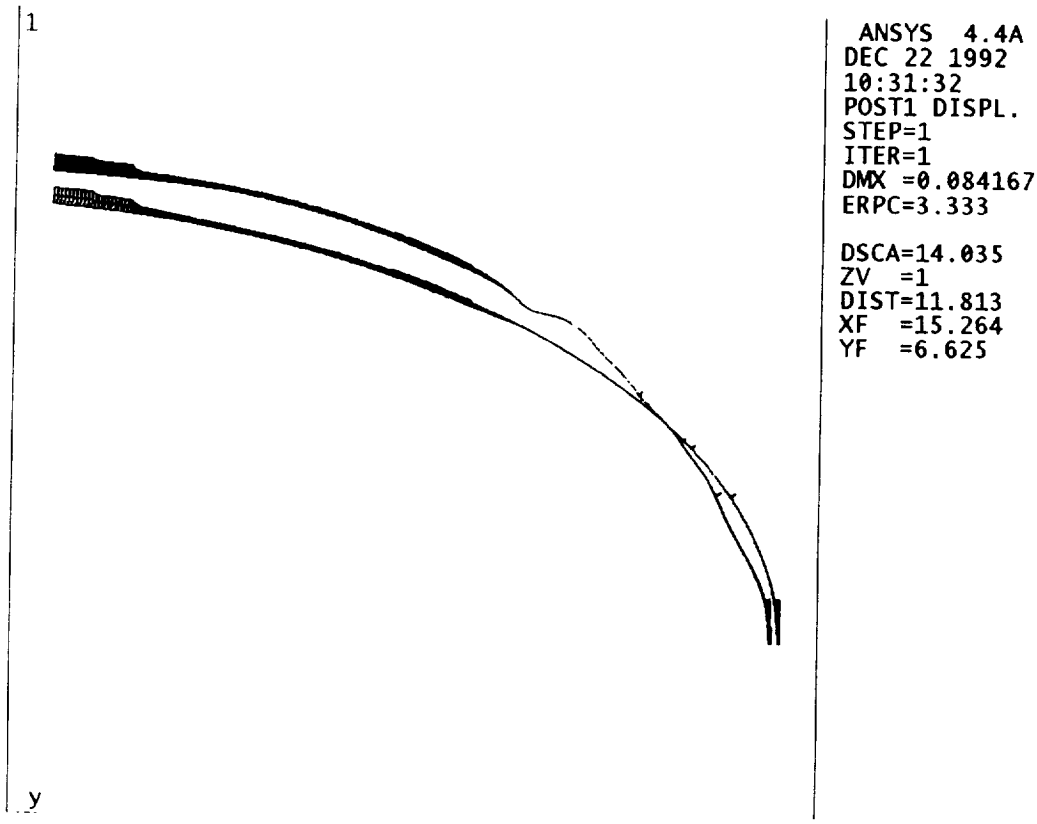

Figure 31. MSFC ANSYS 2–D finite element model showing deformed versus undeformed shapes.

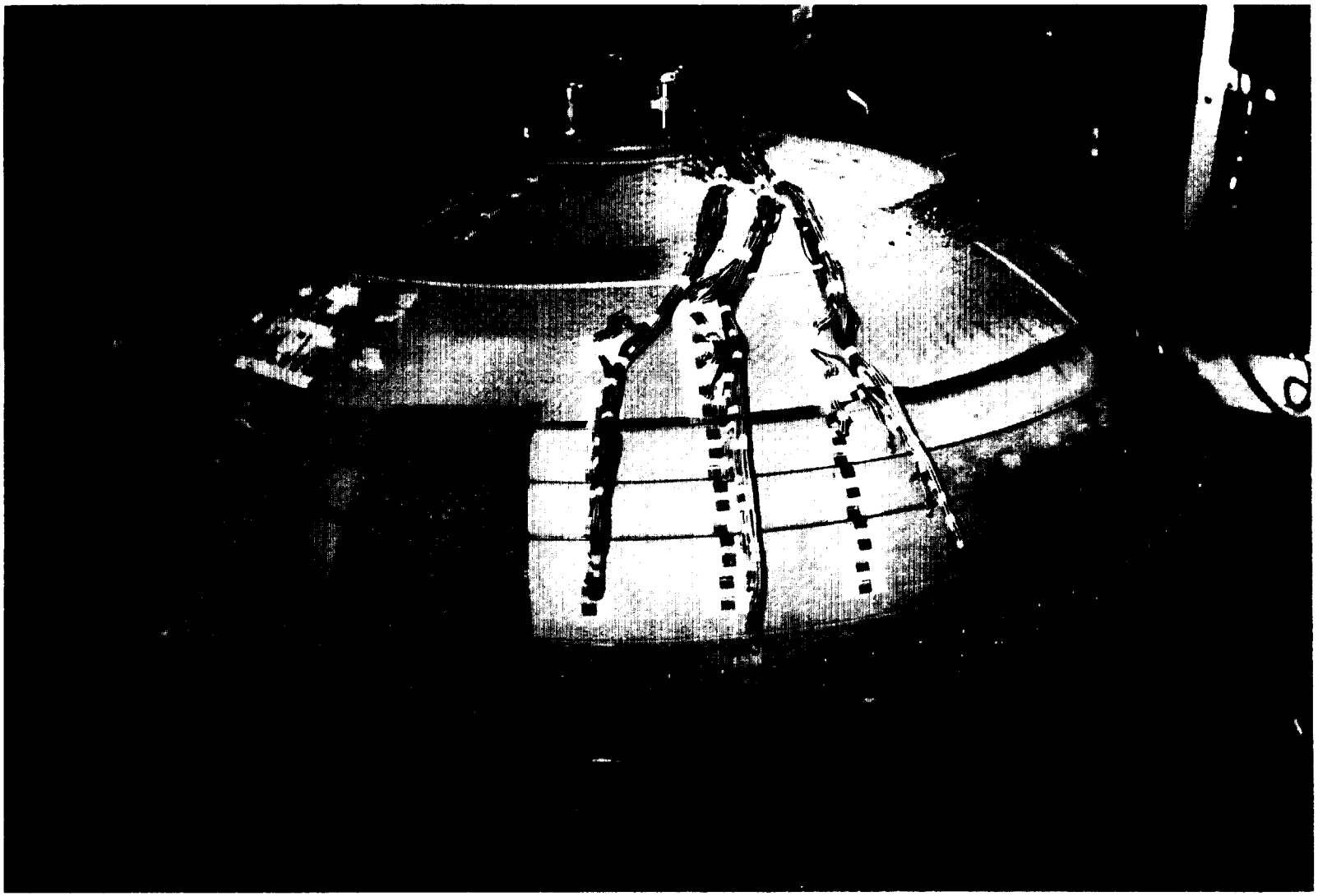

Figure 32. Low-profile dome after failure.

Figure 33. Closeup of failure region.

☆U.S. GOVERNMENT PRINTING OFFICE 1994—533-108/00006

REPORT DOCUMENTATION PAGE

Form Approved
OMB No. 0704-0188

1. AGENCY USE ONLY (Leave blank)	2. REPORT DATE	3. REPORT TYPE AND DATES COVERED
	December 1993	Technical Paper

4. TITLE AND SUBTITLE

Analysis and Test of Low Profile Aluminum Aerospace Tank Dome

5. FUNDING NUMBERS

6. AUTHOR(S)

R. Ahmed and J.M. Wilhelm

7. PERFORMING ORGANIZATION NAME(S) AND ADDRESS(ES)

George C. Marshall Space Flight Center
Marshall Space Flight Center, Alabama 35812

8. PERFORMING ORGANIZATION REPORT NUMBER

M-737

9. SPONSORING/MONITORING AGENCY NAME(S) AND ADDRESS(ES)

National Aeronautics and Space Administration
Washington, DC 20546

10. SPONSORING/MONITORING AGENCY REPORT NUMBER

NASA TP-3442

11. SUPPLEMENTARY NOTES

Prepared by Structures and Dynamics Laboratory, Science and Engineering Directorate.

12a. DISTRIBUTION/AVAILABILITY STATEMENT

Unclassified—Unlimited
Subject Category:39

12b. DISTRIBUTION CODE

13. ABSTRACT *(Maximum 200 words)*

In order to increase the structural performance of cryogenic tanks, the aerospace industry is beginning to employ low-profile bulkheads in new generation launch vehicle designs. This report details the analysis and test of one such dome made from 2219 aluminum. Such domes have two potential failure modes under internal pressure, general tensile failure and hoop compression buckling (in regions near the equator). The test determined the buckling load and ultimate tensile load of the hardware and showed that both compared well with the analysis predictions. This effort was conducted under the auspices of NASA and the General Dynamics Cryogenic Tank Technology Program (CTTP).

14. SUBJECT TERMS

bulkheads, cryogenic tankage, low profile, liquid hydrogen tank, liquid oxygen tank, optimization

15. NUMBER OF PAGES

38

16. PRICE CODE

A03

17. SECURITY CLASSIFICATION OF REPORT	18. SECURITY CLASSIFICATION OF THIS PAGE	19. SECURITY CLASSIFICATION OF ABSTRACT	20. LIMITATION OF ABSTRACT
Unclassified	Unclassified	Unclassified	Unlimited